https://doi.org/10.5194/essd-2026-552
Preprint. Discussion started: 17 August 2026

Open Access Earth System Science Data Discussions

Multi-year ground-based multi-wavelength Raman lidar aerosol dataset over the interior Tibetan Plateau (Yangbajing, 4284 m a.s.l.; 2021–2024)

Yinan Wang[1], Hongxia Cui[1], Wei Zhao[1], Yongheng Bi[1], Tianqi Wang[1] and Daren Lu[1]

[1] Institute of Atmospheric Physics, Chinese Academy of Sciences, Beijing 100029, China.

Correspondence to: Yinan Wang (wangyinan@mail.iap.ac.cn)

Abstract. The interior of the Tibetan Plateau exerts a first-order influence on the Asian monsoon and regional climate, yet vertically resolved aerosol observations there are scarce, and no openly archived, multi-year, ground-based profile record has existed for this exceptionally clean high-altitude environment. We present such a dataset from a six-channel elastic/Raman/depolarisation lidar (355, 387, 408, 532, 607, 1064 nm) at Yangbajing (30.10° N, 90.52° E, 4284 m a.s.l.), covering September 2021 to December 2024: 437 quality-controlled nighttime profiles on a 75 m grid (157 levels, 0.30 to 12 km a.g.l.) and 279 daytime column-AOD retrievals. The independent products are the nitrogen-Raman extinction at 355 and 532 nm and the Raman-derived lidar ratio. The aerosol backscatter at 355 and 532 nm is retrieved by the elastic (Fernald) inversion with an assumed lidar ratio of 50 sr, and the 1064 nm backscatter is a non-independent colour-ratio transfer. Volume and particle depolarisation ratios (532 nm), water vapour mixing ratio (408/387 nm; radiosonde-calibrated C = 90.4 g kg-1, ~17 % uncertainty), Ångström exponents and column aerosol optical depth (AOD) complete the product set, and a scattering-ratio cloud screen supplemented by a particle-depolarisation ice test separates mineral dust from ice. The site is among the cleanest continental settings sampled by lidar: the nighttime detection-night median column AOD at 532 nm is 0.053 (n = 269) and the daytime detection median is 0.078 (n = 208). The Raman-derived site-mean lidar ratio is 51.6 sr (IQR 41 to 80 sr, n = 85), consistent in the median with the assumed 50 sr and with the CALIPSO clean-continental value, but it varies by a factor of two from night to night. This assumption, not photon noise (median relative σ ~1.7 % for the 532 nm extinction, rising to a 90th percentile of ~24 % in the weak-signal upper troposphere), dominates the column-AOD uncertainty (+60 %/-18 %), for which per-profile S = 41 and 80 sr bounds are provided. Daytime AOD tracks AERONET Nam Co (~85 km) in rank order (Pearson r = 0.61, Spearman ρ = 0.72, both $p < 0.001$, n = 41). To our knowledge this is the first openly archived, multi-year, ground-based multi-wavelength aerosol profile dataset from the clean interior Tibetan Plateau, a region pivotal for the Asian monsoon and the Third Pole cryosphere where high surface albedo and complex terrain defeat passive retrievals and leave spaceborne lidar the de facto reference. It supplies the vertically resolved ground truth needed to evaluate and correct spaceborne-lidar aerosol detection and typing, to benchmark next-generation missions such as EarthCARE over bright, high terrain, and to constrain reanalysis, model, and aerosol radiative studies of dust transport and monsoon aerosol over the Third Pole.

https://doi.org/10.5194/essd-2026-552
Preprint. Discussion started: 17 August 2026

Open Access Earth System Science Data Discussions

1 Introduction

The Tibetan Plateau, with a mean elevation exceeding 4000 m a.s.l., exerts a first-order influence on Asian monsoon circulation, regional hydrology, and global climate (Immerzeel et al., 2010; Yao et al., 2012). Aerosol particles over the plateau, including mineral dust transported from the Taklamakan and northern deserts in spring, modulate the regional radiation budget and may accelerate glacier retreat through deposition-driven albedo reduction (Lau et al., 2006; Xu et al., 2020). However, vertically resolved aerosol observations over the plateau interior remain scarce. Spaceborne lidars (CALIOP aboard CALIPSO; Winker et al., 2009) provide global coverage but suffer from limited sensitivity over clean, high-altitude terrain where aerosol loading is low (Kim et al., 2017; Toth et al., 2018; Watson-Parris et al., 2018). Ground-based lidar networks (EARLINET/ACTRIS in Europe, Pappalardo et al., 2014; MPLNET globally; AD-Net in East Asia) have no station in the interior of the Tibetan Plateau, defined here as locations more than 100 km from the plateau edge. Earlier ground-based lidar measurements over the plateau have been either short-term campaigns or edge-of-plateau deployments, and to our knowledge none has been released as an openly archived, multi-year, multi-wavelength record. This leaves a critical gap: no openly archived, multi-year, vertically resolved aerosol ground truth exists for one of the cleanest high-altitude continental environments.

Several studies have characterised aerosol columnar properties over the plateau using sun photometry (Pokharel et al., 2019) or spaceborne retrievals (Huang et al., 2007; Xu et al., 2020), but these lack the vertical resolution needed to evaluate spaceborne lidar detection algorithms or constrain reanalysis aerosol profiles (Zhang et al., 2025). The multi-wavelength Raman lidar used here is part of the Yangbajing atmospheric-profiling facility established by Lu et al. (2018); the present dataset is the first multi-year, quality-controlled aerosol product openly archived from it, and thus realises the long-term observational potential of that facility.

This paper documents a multi-year, multi-wavelength aerosol profile dataset from a ground-based Raman/elastic/depolarisation lidar at Yangbajing (30.10° N, 90.52° E, 4284 m a.s.l.) on the interior Tibetan Plateau. The dataset covers September 2021 to December 2024 and includes 437 quality-controlled nighttime profiles and 279 daytime column-AOD retrievals. Products span three backscatter wavelengths (355, 532, 1064 nm), two extinction wavelengths (355, 532 nm), volume and particle depolarisation ratios (532 nm), water vapour mixing ratio (408/387 nm), Ångström exponents derived from the 355/532 nm pair, and column AOD at 532 nm for both night and day. The vertical caliber of this dataset is as follows: independent extinction (from Raman channels) and lidar ratio are reliable only in the nighttime free troposphere; the boundary layer relies on elastic (Fernald) inversion with an assumed lidar ratio of 50 sr; the 1064 nm backscatter is a non-independent colour-ratio transfer, not an independent retrieval. These boundaries are described in Sect. 3 and stated explicitly in the dataset metadata.

We document the instrument, retrieval methods, quality control, uncertainty budget, and independent corroboration, so that the dataset can be used for the evaluation of spaceborne-lidar detection and aerosol

https://doi.org/10.5194/essd-2026-552
Preprint. Discussion started: 17 August 2026

typing, reanalysis and model evaluation, radiative-transfer calculations, and aerosol climate studies over the Third Pole.

2 Site and instrument

2.1 Site and aerosol environment

The lidar is operated at the Yangbajing Whole-Atmosphere Observatory (30.102° N, 90.522° E, 4284 m a.s.l.), located on the interior Tibetan Plateau approximately 90 km northwest of Lhasa (Fig. 1). The site lies more than 100 km from the nearest plateau edge in all directions, placing it firmly within the plateau interior. Zhao et al. (2024) used co-located lidar and radar observations at this site to characterise cloud vertical structures over the interior plateau. The surrounding terrain is a broad valley (the Damxung basin) flanked by mountains exceeding 5500 m. The high elevation means that the lidar operates above a substantial fraction of the tropospheric column, and the local aerosol environment is among the cleanest continental settings: the nighttime detection-night median column AOD at 532 nm is 0.053. The prevailing aerosol regime is background continental in autumn and winter, transitioning to a dust-influenced regime in spring (March to May), when long-range-transported mineral dust from the Taklamakan and northern deserts, together with contributions from local dust emissions, produces the seasonal AOD maximum.

2.2 Multi-wavelength Raman lidar system

The lidar is the multi-wavelength Raman/elastic/depolarisation system of the Yangbajing atmospheric-profiling facility (Lu et al., 2018), built around a 400 mm diameter Cassegrain telescope (Fig. 2). The transmitter uses a pulsed Nd:YAG laser emitting at 355 nm (third harmonic), 532 nm (second harmonic), and 1064 nm (fundamental), with a repetition rate of 20 Hz. The receiver comprises six detection channels (Table 1): (1) Elastic backscatter at 355 nm. (2) Nitrogen vibrational Raman at 387 nm (excited by 355 nm). (3) Water vapour vibrational Raman at 408 nm (excited by 355 nm). (4) Elastic backscatter at 532 nm, with a polarising beamsplitter separating co-polarised (parallel) and cross-polarised (perpendicular) components for depolarisation measurement. (5) Nitrogen vibrational Raman at 607 nm (excited by 532 nm). (6) Elastic backscatter at 1064 nm.

The 355, 387, 408, 532, and 607 nm channels use photomultiplier tubes (PMTs) operating in both analogue and photon-counting modes; the 1064 nm channel uses an avalanche photodiode (APD) in analogue mode. Raw profiles are acquired at 3.75 m range resolution and 60 s temporal resolution (1200 laser shots at 20 Hz) by a Licel transient recorder. The instrument specifications are summarised in Table 1.

Table 1. Instrument channel specifications.

https://doi.org/10.5194/essd-2026-552
Preprint. Discussion started: 17 August 2026

Channel	Wavelength (nm)	Detection	Signal source	Detector	Mode
Elastic	355	Backscatter	Aerosol + molecular	PMT	AN + PC
N_2 Raman	387	Inelastic	N_2 vibrational (from 355)	PMT	AN + PC
H_2O Raman	408	Inelastic	H_2O vibrational (from 355)	PMT	AN + PC
Elastic (parallel)	532	Backscatter	Aerosol + molecular (co-pol.)	PMT	AN + PC
Elastic (cross)	532	Backscatter	Aerosol + molecular (cross-pol.)	PMT	AN + PC
N_2 Raman	607	Inelastic	N_2 vibrational (from 532)	PMT	AN + PC
Elastic	1064	Backscatter	Aerosol + molecular	APD	AN

AN: analogue; PC: photon-counting.

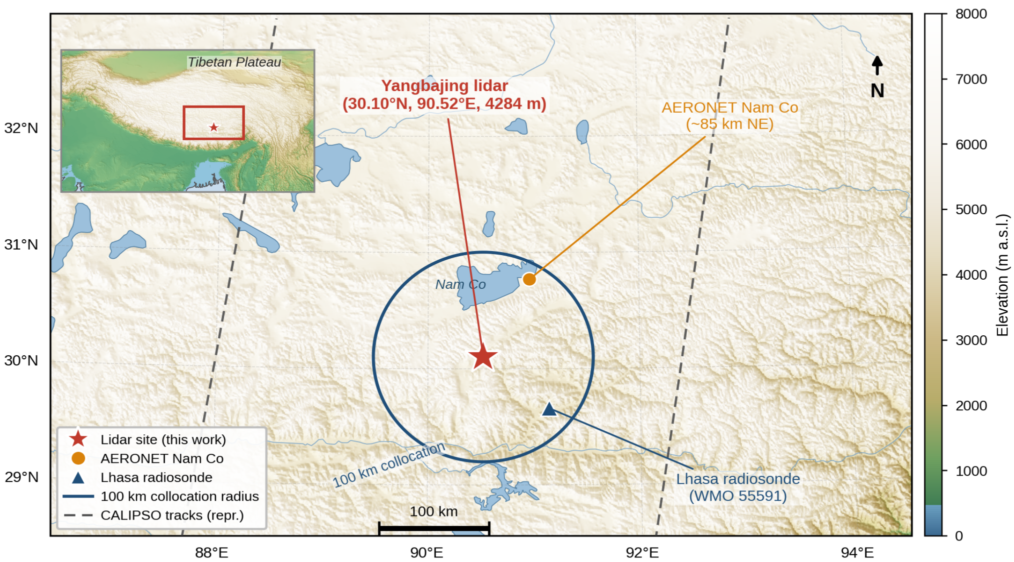

https://doi.org/10.5194/essd-2026-552
Preprint. Discussion started: 17 August 2026

Figure 1. Location of the Yangbajing multi-wavelength lidar (red star; 30.10° N, 90.52° E, 4284 m a.s.l.) on the interior Tibetan Plateau, more than 100 km from the nearest plateau edge. Also shown are the AERONET Nam Co sun photometer (~85 km NE), the Lhasa radiosonde station (WMO 55591), Nam Co lake, the 100 km collocation radius used for CALIPSO and AERONET comparison, and representative CALIPSO ground tracks. Colour shading gives terrain elevation (colour bar, right). Inset: the site within the Tibetan Plateau and Asia, with the main-map extent boxed in red. Albers equal-area projection. CALIPSO data © NASA/CNES. AERONET data © NASA GSFC.

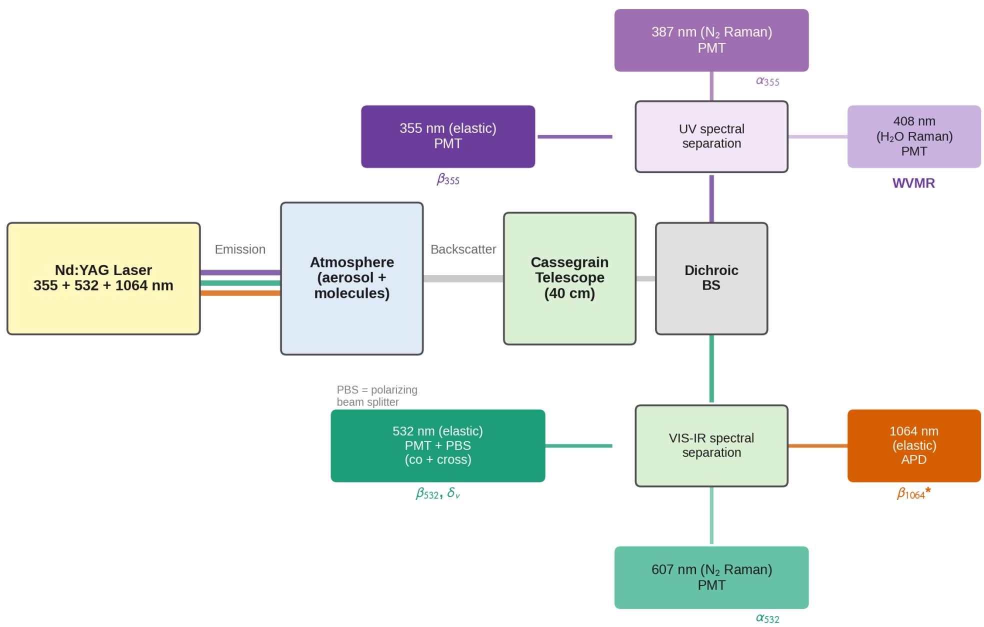

Figure 2. Optical layout of the multi-wavelength Raman lidar. The Nd:YAG laser emits at 355, 532 and 1064 nm; backscattered light is collected by a 400 mm Cassegrain telescope and split by a dichroic beamsplitter into a UV arm (355 nm elastic → β355; 387 nm N2 Raman → α355; 408 nm H2O Raman → WVMR) and a visible–infrared arm (532 nm elastic with a polarising beamsplitter for co- and cross-polarised detection → β532, δv; 607 nm N2 Raman → α532; 1064 nm elastic on an APD → β1064*). β1064* denotes the non-independent colour-ratio transfer product. Detector-box colours identify the two arms.

3 Data and methods

Following common practice for lidar data archives (D'Amico et al., 2015), the dataset is organised into three processing levels. Level 0 (L0) is the raw Licel signal as recorded (3.75 m, 60 s, analogue and photon-counting), uncorrected and uncalibrated. Level 1 (L1) is the instrument-corrected, cloud-screened, nightly-averaged signal on the native range grid, after dark-current, dead-time, and background subtraction, analogue/photon-counting gluing, and range-squared correction. Level 2 (L2) comprises the retrieved

https://doi.org/10.5194/essd-2026-552
Preprint. Discussion started: 17 August 2026

geophysical products on the uniform 75 m grid: backscatter at 355, 532, and 1064 nm, extinction at 355 and 532 nm, volume depolarisation at 532 nm, water vapour mixing ratio, Ångström exponents, and column AOD, each accompanied by a per-bin uncertainty and quality flags. Only the Level-2 products are archived (see the Data availability statement); the Level-0 and Level-1 signals are available from the corresponding author on request. Sect. 3.1 describes the L0-to-L1 signal processing; Sect. 3.2 to 3.8 describe the L1-to-L2 retrievals in turn.

3.1 Signal pre-processing and nightly averaging

Raw Licel profiles are acquired at 3.75 m range resolution and 60 s temporal integration (1200 shots at 20 Hz). The processing chain follows established practice (D'Amico et al., 2015; Mattis et al., 2016) with two site-specific adaptations: (a) explicit dark-current (DARK-profile) subtraction is required because the low aerosol signal levels at 4284 m make residual signal-induced noise non-negligible, and (b) nightly integration times of 2 to 6 hours are needed to achieve adequate SNR in the Raman channels. Pre-processing includes: (i) dark-current subtraction from each channel; (ii) dead-time correction for photon-counting channels; (iii) background subtraction using the signal in the 50 to 60 km range window; (iv) gluing of analogue and photon-counting signals in the overlap zone (typically 2 to 5 km range), using a signal-dependent threshold to select the optimal transition altitude on each profile; (v) range-squared correction; and (vi) temporal averaging to nightly-mean profiles (typically 2 to 6 hours of integration per night). The nightly mean is set by the extremely low aerosol loading at this clean, high-altitude site: the weak nitrogen-Raman return requires 2 to 6 hours of integration for an adequate signal-to-noise ratio in the extinction retrieval, so a single nightly profile, rather than a finer time series, is the science-grade multi-wavelength product that the Raman signal supports. Where the aerosol layering evolves slowly through the night, as in the example of Fig. 3a,b, this nightly mean is also representative of the instantaneous state. Molecular backscatter and extinction profiles are computed from the US Standard Atmosphere 1976 temperature profile scaled to the measured surface pressure at the site (4284 m a.s.l.). Because each retrieval is normalised to the molecular signal at an aerosol-free reference altitude, it is primarily sensitive to the shape of the molecular profile rather than its absolute value; the residual sensitivity to the assumed temperature structure is small compared with the lidar-ratio systematic that dominates the uncertainty budget (Sect. 5.2). Substituting the Lhasa radiosonde temperature profile (WMO 55591, ~90 km distant and 634 m lower) or a reanalysis profile for the standard atmosphere is a minor refinement, noted for future versions.

The processed profiles are gridded onto a uniform 75 m altitude grid from 0.30 to 12 km above ground level (a.g.l.), yielding 157 vertical levels. The effective vertical resolution is coarser than the 75 m grid for the Raman extinction, where it is altitude-dependent (Sect. 3.4), and is approximately the grid spacing for the elastic backscatter channels.

https://doi.org/10.5194/essd-2026-552
Preprint. Discussion started: 17 August 2026

3.2 Elastic backscatter retrieval at 355 and 532 nm

Aerosol backscatter coefficients at 355 and 532 nm are retrieved by the Fernald (1984) backward integration method. The inversion requires an assumed lidar ratio (extinction-to-backscatter ratio, S). We apply a fixed S = 50 sr uniformly to all profiles at both wavelengths. Although the lidar ratio is in general wavelength-dependent, the nitrogen-Raman lidar ratios retrieved here at 355 and 532 nm show no significant systematic difference on the nights where both are retrievable (median per-night 532-minus-355 nm difference about 3 sr; interquartile range -7 to +21 sr, Wilcoxon signed-rank p = 0.16, n = 30 paired nights), so a common value at the two wavelengths is a reasonable approximation, and any residual wavelength dependence is absorbed into the lidar-ratio uncertainty (Sect. 5.2). The boundary condition is set at the uppermost altitude bin where the signal-to-noise ratio exceeds 3, where the total backscatter is assumed equal to the molecular backscatter (aerosol-free reference). This reference altitude varies from night to night depending on the SNR profile, typically falling between 9 and 12 km a.g.l. The sensitivity of the retrieved backscatter to the lidar-ratio assumption is discussed in Sect. 5.2. Residual aerosol at the reference altitude would bias the column AOD low; since any such aerosol is below the 5 Mm^{-1} extinction detection limit and confined to a layer of order 1 to 2 km near the reference, its contribution is bounded by the product of that detection-floor extinction and a 1 to 2 km layer thickness, about 0.005 to 0.01 in column AOD, comparable to the detection floor and small relative to the lidar-ratio systematic. The Rayleigh-normalised reference fit is stable, with a night-to-night relative standard deviation of about 1.6 %.

A fixed lidar ratio, rather than the per-night Raman value, is used for the elastic backscatter. The Raman lidar ratio is retrievable only at night, only in the free troposphere, and only on the subset of nights with adequate aerosol signal (85 nights; Sect. 3.4), so it cannot supply an all-night, all-altitude, two-wavelength constraint. At this exceptionally clean site the self-calibrated elastic/Raman backscatter retrieval that would remove the lidar-ratio assumption altogether (the Raman backscatter method of Ansmann et al., 1992) is dominated by noise, as quantified in Sect. 10. Retrieving the aerosol backscatter with the elastic (Fernald) inversion under an assumed lidar ratio, and reporting the Raman-derived lidar ratio separately as an independent characterisation, is the standard low-signal practice of ground-based Raman-lidar networks; it corresponds to the elastic backscatter and the Raman extinction products of the EARLINET Single Calculus Chain (D'Amico et al., 2015; Mattis et al., 2016). Users should therefore treat the aerosol backscatter and column AOD as conditional on the assumed lidar ratio, whereas the Raman extinction and the lidar ratio are independent of it; the resulting AOD sensitivity is quantified in Sect. 5.2 and provided as per-profile bounds.

The elastic backscatter products have per-night availability of ~68 % (355 nm) and ~70 % (532 nm) across the 437 nights, reflecting the signal-to-noise-based detection limit (Sect. 4.3). The Fernald inversion and the selection of the aerosol-free reference altitude are illustrated for a representative night in Fig. S2.

https://doi.org/10.5194/essd-2026-552
Preprint. Discussion started: 17 August 2026

Open Access Earth System Science Data Discussions

3.3 Backscatter at 1064 nm: colour-ratio transfer

The 1064 nm channel provides elastic backscatter only; no Raman channel exists at a wavelength suitable for independent extinction retrieval at 1064 nm. We retrieve the 1064 nm aerosol backscatter coefficient by colour-ratio transfer from the 532 nm backscatter:

$$\beta_{aer}(1064) = \beta_{aer}(532) \times (532/1064)^{k} = \beta_{aer}(532) \times 0.5^{k}, \quad (1)$$

where k is the backscatter-related Ångström exponent. We assume k = 1, yielding $\beta_{aer}(1064) = \beta_{aer}(532) \times 0.5$.

This product is explicitly non-independent: it inherits all uncertainties of the 532 nm backscatter and adds the assumption that the backscatter Ångström exponent equals unity. The assumption k = 1 is a rough approximation; dust-dominated aerosol (k ~ 0) and fine-mode pollution (k > 1) deviate from it. Because the transfer factor is 0.5 raised to the power k, under strong dust (k = 0) the true 1064 nm backscatter equals the 532 nm value rather than half of it, a factor of two above the archived product, while for fine-mode pollution (k about 1.5) it is about 30 percent below; the product is therefore accurate only to about a factor of two in strong dust. The 1064 nm backscatter is provided only in bins where the 532 nm backscatter exceeds the detection limit, and only in aerosol layers of sufficient strength. Users should treat this product as a non-independent colour-ratio estimate, not an independent measurement.

3.4 Raman extinction retrieval at 355 and 532 nm, and lidar ratio

Aerosol extinction coefficients at 355 and 532 nm are retrieved from the nitrogen Raman channels at 387 and 607 nm, respectively, using the standard derivative method (Ansmann et al., 1990). The Raman-derived extinction is independent of the lidar ratio, relying only on the known Raman scattering cross-section, the molecular number density profile, and the wavelength dependence of molecular (Rayleigh) extinction between the excitation and Raman wavelengths. The correction for this wavelength-dependent molecular transmission uses an Ångström exponent of 1, which accounts for the differential Rayleigh scattering at the excitation and Raman-shifted wavelengths; this is the standard molecular transmission correction, not an aerosol-type assumption.

The derivative is computed by a Savitzky-Golay filter whose smoothing window is widened with altitude to preserve the signal-to-noise ratio in the weak Raman return. The effective vertical resolution (Iarlori et al., 2015) is therefore coarser than the 75 m grid and increases with height: the smoothing half-window widens from about 125 m near the surface to about 600 m in the upper troposphere, giving an effective vertical resolution of approximately 250 m at 0.5 km, 500 m at 2 km, and 1.2 km at 6 km a.g.l. Comparisons with other datasets should use this effective resolution rather than the grid spacing. A bin-level absolute detection threshold (ADET) of 5 Mm^{-1} is applied: bins with retrieved extinction below this threshold are treated as

https://doi.org/10.5194/essd-2026-552
Preprint. Discussion started: 17 August 2026

below detection and set to _FillValue (masked) in the gridded file, rather than retained as their noisy or negative values. The Raman derivative method and the detection gate are illustrated in Fig. S3.

The Raman extinction is reliable only at night, when the solar background is negligible, and only in the free troposphere, above the region where incomplete geometric overlap degrades the inversion. In the boundary layer (the lowest ~0.6 km a.g.l.), the Raman signal-to-noise ratio is insufficient for a reliable derivative, and the extinction there is effectively that of the elastic (Fernald) retrieval.

From the independently retrieved extinction and backscatter at the same wavelength, the lidar ratio is computed as $S = \alpha/\beta$. The site-mean climatological lidar ratio is 51.6 sr (IQR 41 to 80 sr, n = 85 adequate-signal nights after quality control on the extinction Ångström exponent, threshold >= -0.2). The IQR spans approximately a factor of two, reflecting real variability in aerosol type across nights. The seasonal medians are 46 sr (DJF), 50 sr (MAM), 61 sr (JJA), and 51 sr (SON). The CALIPSO Version 4 lidar-ratio prior for the "clean continental" type in this region is 51.7 to 56.9 sr (Kim et al., 2018), consistent in the median with our Raman-derived value; it is the night-to-night variability, not the choice of a single reference value near 50 sr, that dominates the column-AOD uncertainty (Sect. 5.2). Per-bin lidar ratios are too noisy for publication and are not included in the dataset.

3.5 Volume depolarisation ratio at 532 nm

The volume linear depolarisation ratio at 532 nm (δ_v; hereafter volume depolarisation ratio) is defined as the ratio of the cross-polarised to the co-polarised elastic backscatter signal, corrected for the polarisation characteristics of the receiver optics:

$$\delta_v = (\text{signal\_cross} \,/\, \text{signal\_parallel}) \times V^*, \quad (2)$$

where V is the gain-ratio calibration factor. V corrects only for the differential gain between the cross and parallel detection channels; it does not incorporate the full polarisation model of Freudenthaler (2016), which accounts for receiver-optics diattenuation. Neglecting this diattenuation is a known approximation that may introduce a small systematic bias in δ_v, particularly at low depolarisation values.

The dataset spans three calibration epochs. The 2021 epoch (64 nights) has no absolute depolarisation calibration: the gain ratio between the cross and parallel channels is set to unity (V = 1), so the volume depolarisation for these nights is not released as values but is set to _FillValue throughout, the flag depol_calibration = 0 documenting why, and these nights cannot be used quantitatively even inadvertently, a known limitation of the early observation period. On the 365 nights of the HV-gain lookup-table epoch (depol_calibration = 1), the gain ratio is taken from a laboratory-measured high-voltage-versus-gain LUT for each photomultiplier; we quantify its uncertainty by cross-validating the HV-gain law against the nine +/-45 degree calibration measurements in a leave-one-out test, which gives an absolute RMS error of 0.063 in the predicted gain ratio V ($R^2 = 0.999$ for the analogue-mode gain ratio used in the product). Because the volume

https://doi.org/10.5194/essd-2026-552
Preprint. Discussion started: 17 August 2026

Open Access Earth System Science Data Discussions

depolarisation ratio scales inversely with the gain ratio, the relative calibration uncertainty is σ_{V*} / V; across the HV-LUT nights, whose gain ratios span 2.3 to 9.2 (the same range as the calibration nights, so this is an interpolation rather than an extrapolation), it has a median of ~1.3 % and a per-night range of 0.7 to 2.8 %. This gain-law term captures only the precision of the gain-ratio prediction; it does not include the receiver diattenuation neglected by the gain-only V model (described above). We bound that residual receiver term empirically from the clean molecular reference layer. The molecular volume linear depolarisation ratio is about 0.004 for a narrow (Cabannes) passband and larger for a broader passband (Behrendt and Nakamura, 2002); the calibrated product yields about 0.0065 there. Conservatively attributing the full excess over the narrow-band value to the receiver gives an upper bound on the residual receiver systematic (diattenuation plus finite polarising-beamsplitter extinction) of about +0.002 in absolute δ_v, part of which may instead reflect the true broadened-passband molecular depolarisation. This residual dominates at low depolarisation, corresponding to about 10 % at background values ($\delta_v \sim 0.02$) but below 2 % for dust layers ($\delta_v > 0.1$). The gain law and the resulting per-night calibration uncertainty are shown in Fig. S4. The most accurate calibration is that of the direct +/-45 degree nights (depol_calibration = 2; eight of the calibration measurements also pass the science-night quality control and are archived with this flag), where the gain ratio is measured in situ by rotating a half-wave plate to +45 and -45 degrees (the Delta-90 method; Freudenthaler, 2016).

The per-night availability of the depolarisation product is ~85 % of the 437 nights; the 64 uncalibrated 2021 nights carry no calibrated depolarisation and account for most of the shortfall. Taken over all detected aerosol bins, the median volume depolarisation ratio is 0.057 (IQR 0.022 to 0.119); the 1 to 5 km layer-mean used for aerosol typing in Sect. 6.2 has a slightly lower median (0.047), reflecting the different averaging. Dust layers produce δ_v of order 0.1 to 0.3, and ice layers higher still. In addition to the volume depolarisation, the particle linear depolarisation ratio δ_p is archived where it can be reliably retrieved (R >= 2.5 and calibrated depolarisation), computed from the volume depolarisation and the backscatter ratio with an effective molecular depolarisation of 0.0065. This 0.0065 includes the small unquantified receiver excess over the true molecular value (Sect. 3.5); using it as the molecular reference biases the retrieved δ_p slightly low, so the archived δ_p is a conservative estimate for weakly depolarising layers and does not raise the risk of misclassifying dust as ice. Because the particle depolarisation of mineral dust cannot exceed about 0.40 whereas ice reaches 0.45 to 0.8, δ_p is the primary dust-versus-ice discriminant and underpins the ice screening (Sect. 4.1) and aerosol typing (Sect. 6.2); classification within the narrow 0.40 to 0.45 overlap band is inherently uncertain, within the combined calibration and retrieval error, and layers there should be treated as ambiguous.

3.6 Water-vapour mixing ratio retrieval and calibration

The water vapour mixing ratio (WVMR) is retrieved from the ratio of the water vapour Raman signal at 408 nm to the nitrogen Raman signal at 387 nm:

https://doi.org/10.5194/essd-2026-552
Preprint. Discussion started: 17 August 2026

Earth System Science Data Discussions
Open Access

$$\mathrm{WVMR} = C \times (P\_408 / P\_387), \quad (3)$$

where P_408 and P_387 are the range-corrected, background-subtracted Raman signals and C is a calibration constant determined by comparison with co-located radiosonde profiles.

The calibration constant is obtained by transfer from radiosonde profiles at Lhasa (WMO station 55591, IGRA2 database), located ~90 km to the southeast at 3650 m a.s.l. (great-circle ground distance), 634 m lower than the lidar. The radiosonde comparison uses 315 nights with temporal coincidence within 3 hours of the 00 and 12 UTC launches. The resulting calibration constant is C = 90.4 g kg^{-1} with an estimated uncertainty of ~17 %. This figure is a conservative estimate: it is the full spread of the night-to-night transfer constant, which includes the radiosonde sensor accuracy, the spatial-representativeness error (the two sites are ~90 km apart), and the temporal mismatch, and therefore bounds the calibration uncertainty from above rather than isolating the lidar contribution alone.

The surface-level median WVMR is 2.89 g kg^{-1} (range 0.17 to 12 g kg^{-1} across all nights), reflecting the extremely dry conditions at 4284 m a.s.l. In 98 % of profiles, the WVMR decreases with altitude (negative overall gradient), as expected from the Clausius-Clapeyron relation and the decreasing temperature with height. Bin-level availability is ~99 %.

3.7 Grid and effective resolution

All products are archived on a common vertical grid of 157 levels from 0.30 to 12 km a.g.l. (approximately 4584 to 16284 m a.s.l.) at 75 m spacing. The effective vertical resolution depends on the product: for the Raman extinction it is coarser than the grid and increases with altitude (Sect. 3.4), whereas for backscatter and depolarisation (elastic) it is approximately the grid spacing (~75 m). The temporal resolution is one nightly-mean profile per night.

3.8 Daytime column AOD from atmospheric transmittance

By day, the solar background prevents reliable Raman and high-altitude elastic retrievals, so the daytime product is restricted to the column aerosol optical depth at 532 nm. It is obtained by a transmittance-ratio method: the two-way aerosol transmittance across the column is derived from the range-corrected elastic 532 nm signal relative to the expected molecular (Rayleigh) signal between a near-surface reference and a clean reference altitude above the aerosol layer, and the column AOD follows as minus one half of the natural logarithm of this transmittance. Anchoring to the column transmittance greatly reduces the dependence on the assumed lidar ratio relative to the nighttime Fernald profiles, but a residual dependence remains in the near-field portion below the lower reference, so the same conservative fractional lidar-ratio envelope as at night (the S = 41 and 80 sr bounds, column_aod_532_day_S41/S80) is provided to bound it. The same detection-limit treatment as for the nighttime AOD (Sect. 4.3) is applied: days below the detection limit are

https://doi.org/10.5194/essd-2026-552
Preprint. Discussion started: 17 August 2026

flagged rather than reported as point values. Daytime products carry their own time dimension (column_aod_532_day; 279 days, 208 detections, detection median 0.078).

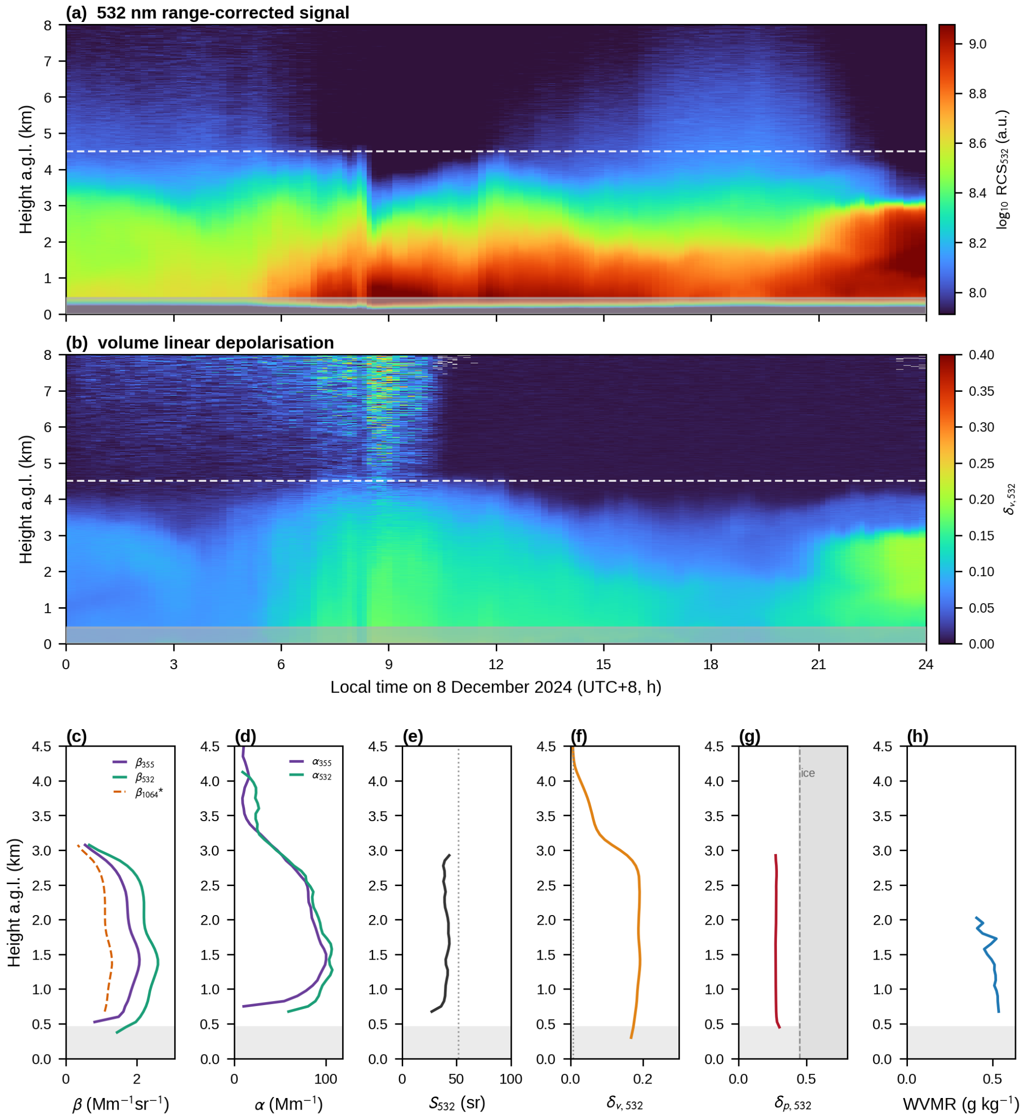

Figure 3. Multi-wavelength showcase of a well-observed Asian mineral-dust event over Yangbajing (8 December 2024). (a) Whole-night time-height evolution of the 532 nm range-corrected signal and (b) the calibrated volume linear depolarisation ratio (8-min blocks; signal-to-noise-limited bins masked grey; dashed line marks the 4.5 km display top of the profiles below), showing a persistent, semi-transparent dust layer below ~3 km a.g.l. through the night. (c)–(h) Nightly-mean profiles: (c) aerosol backscatter at 355, 532 and 1064 nm; (d) aerosol extinction at 355 and 532 nm (N_2-Raman); (e) 532 nm lidar ratio S = α/β (dotted line, climatological 51.6 sr; layer S ≈ 41 sr,

https://doi.org/10.5194/essd-2026-552
Preprint. Discussion started: 17 August 2026

Open Access Earth System Science Data Discussions

characteristic of dust); (f) volume depolarisation (dotted line, molecular value); (g) particle linear depolarisation δ_p, with the ice regime (δ_p > 0.45) shaded; the layer $\delta_p \approx 0.27$ lies firmly in the mineral-dust range, confirming dust rather than ice; (h) water-vapour mixing ratio. The grey band marks the incomplete-overlap zone (<0.45 km a.g.l.); β1064 is the non-independent colour-ratio transfer product.

4 Quality control

4.1 Cloud screening

Cloud contamination is identified from the 532 nm scattering ratio R = βtotal / βmolecular (aerosol-plus-molecular backscatter relative to the molecular profile) and the volume depolarisation ratio, evaluated on each nightly retrieval within the aerosol column (0.45 km a.g.l. to the aerosol-free reference altitude). Two complementary criteria are applied. (i) Dense clouds (liquid-water clouds and optically thick cirrus) are flagged where R exceeds 10 over at least two consecutive range bins. This threshold is supported by the data themselves: at this clean, high-altitude site the peak-layer scattering ratio of aerosol layers stays at or below R ≈ 10 across the whole record (95th percentile 8.9, maximum 10.0), whereas dense clouds exceed it (the fifth percentile of the cloud peak-layer R is 10.6). Because R > 10 is itself one of the criteria that define the dense-cloud class, the fact that no aerosol night crosses the gate is in part a consistency check rather than a fully independent validation; its physical content is that the peak scattering ratio of the aerosol population tops out just below the gate (maximum 10.0) while the dense-cloud population begins above it (fifth percentile 10.6), the ice points below R = 10 in Fig. S1 being accounted for by the independent depolarisation-temperature and particle-depolarisation criteria rather than by the R gate. Thin cirrus can have a much lower peak scattering ratio (down to R ≈ 3) and is not captured by this gate; it is instead flagged by the cirrus criterion (ii) below, so the two criteria are complementary. (ii) Thin cold cirrus (semi-transparent ice with R < 10) is flagged where a localised peak in R coincides with strong depolarisation (volume depolarisation exceeding 0.2) and a temperature below −40 °C (from the molecular temperature profile, below the −38 °C homogeneous-freezing level). (iii) Because the free troposphere above the 4284 m plateau is cold even a short height above the surface, ice frequently forms in the mixed-phase regime well above −40 °C and would be missed by (ii); such warm ice is identified from the particle linear depolarisation ratio δp (Sect. 3.5, 6.2), which cannot exceed about 0.40 for mineral dust. A sustained layer (at least three bins at R >= 2.5) with δp > 0.45 is therefore flagged as ice at any temperature, and mineral dust (δp ~ 0.25 to 0.40) is separated from ice (δp > 0.45). Criteria (ii) and (iii) follow the ice-cloud region of the (scattering-ratio, depolarisation, temperature) feature space used by the CALIPSO cloud-aerosol discrimination scheme (Vaughan et al., 2009; Liu et al., 2019) and the ice-cloud identification of Sassen and Cho (1992).

The night-level flag cloud_free_night is defined for usability: a night is retained as cloud-free-for-aerosol (cloud_free_night = 1) when it is clear or carries only thin cirrus above 5 km a.g.l., so that the aerosol column beneath is unaffected; it is set to cloud-affected (0) only when a cloud contaminates the aerosol layer (cloud

https://doi.org/10.5194/essd-2026-552
Preprint. Discussion started: 17 August 2026

base below 5 km a.g.l.) or fills more than half of the usable column. Of the 437 quality-controlled nights (from 460 candidates), 284 are cloud-free-for-aerosol and 153 are cloud-affected; a cloud layer of some kind is detected on 169 nights (the 16-night difference is thin cirrus above 5 km a.g.l. that does not contaminate the aerosol column below). The per-night cloud information is archived as separate variables (Sect. 8.2), namely cloud_detected, the cloud-base and cloud-top heights, and the thermodynamic phase (liquid water on 10 nights, ice on 40, undetermined on 119), so that users requiring stricter clearing can apply their own criteria. Where a cloud is detected, the column aerosol optical depth is integrated only below the cloud base.

An elastic-plus-depolarisation lidar alone cannot in every case separate a dense, warm, spherical layer (a liquid water cloud) from an exceptionally dense spherical aerosol; we adopt the conservative scattering-ratio gate above and provide the per-night flags so that this residual ambiguity is transparent. Cirrus occurring outside the nightly retrieval window is not captured by the per-night screen. This scattering-ratio screen replaces an earlier depolarisation-saturation mask and, unlike a fixed δ_v threshold, does not misclassify strongly depolarising dust as cloud.

4.2 Overlap correction and near-field exclusion

The geometric overlap function of the lidar was determined experimentally from the nitrogen-Raman channels following Wandinger and Ansmann (2002), using an ensemble of 40 clean nights (column AOD at 532 nm below 0.05) and normalising the Raman-to-molecular signal ratio in the aerosol-free 3 to 5 km layer. The overlap reaches unity by 0.45 km a.g.l. at 532 nm and by 0.68 km a.g.l. at 355 nm (Fig. S6). The full-overlap height differs between the two wavelengths because each is directed onto its own field stop and interference filter behind the achromatic reflective telescope, rather than through telescope chromatic aberration; this channel-to-channel difference is robust to the Raman signal-to-noise ratio (restricting the ensemble to the higher-signal half of the nights leaves the 355 nm full-overlap height unchanged; see Table S1) and follows the standard assumption that the elastic and nitrogen-Raman overlap functions are identical (Wandinger and Ansmann, 2002; Comeron et al., 2023). The elastic aerosol backscatter coefficients at 355 and 532 nm, and the colour-ratio 1064 nm product derived from them, are divided by this overlap function; the two overlap profiles are archived as ancillary variables (overlap_355, overlap_532). Below the height at which the overlap falls under 0.5 the correction is no longer reliable, so those lowest bins (the 0.30 km bin at 532 nm and the bins below 0.53 km at 355 nm) are set to _FillValue. The Raman extinction retrieval, which uses the derivative of the logarithm of the signal ratio, remains more sensitive to residual overlap error and is therefore reported only in the free troposphere above the full-overlap height.

4.3 Signal-to-noise ratio and detection limits

Each bin in each product is subject to a signal-to-noise ratio (SNR) check. Bins with SNR below a product-specific threshold are flagged as below-detection. The per-night availability percentages reported in Sect. 3

https://doi.org/10.5194/essd-2026-552
Preprint. Discussion started: 17 August 2026

Open Access Earth System Science Data Discussions

(e.g. ~98 % for Raman extinction, ~70 % for elastic backscatter at 532 nm) give the fraction of the 437 nights on which the product yields at least one valid bin, not the fraction of individual bins retained; the per-bin detection is much sparser, particularly in the free troposphere, where the Raman extinction is retrievable on only 22 to 64 % of nights above 2 km (Sect. 6.1). The column AOD, which requires enough signal through the aerosol layer to integrate, is accordingly detected on fewer nights (62 %) than the ~98 % per-night extinction availability. The detection limits are published as per-bin flags in the dataset. For the Raman extinction, an absolute detection threshold (ADET) of 5 Mm^{-1} is additionally applied: bins below it, where the retrieved extinction would be noise-dominated, are set to _FillValue (masked; Sect. 3.4) rather than retained as noisy values.

4.4 607 nm elastic crosstalk diagnosis and flagging

The 607 nm nitrogen Raman channel is susceptible to elastic-signal leakage (crosstalk) on nights with strong aerosol backscatter at 532 nm. The physical mechanism is that a fraction of the intense 532 nm elastic return passes through the 607 nm interference filter, contaminating the Raman signal. This artefact affects primarily strong-dust nights in spring and late winter.

The archived leak607_crosstalk_flag is set by a per-night linear regression, over the 0.8 to 4.5 km range, of the corrected 607/387 signal ratio against an in-band 532 nm elastic-leak proxy, with an altitude term; the t-statistic is the ratio of the fitted leak coefficient to its standard error, and a night is flagged where $t > 3$ (a leak coefficient significantly different from zero at better than the three-standard-error level, a regression-slope significance test). The ratio of the apparent 607 nm aerosol optical depth to the 532 nm elastic AOD provides a simpler first indication: it is near unity (0.8 to 1.3) on uncontaminated nights and exceeds 2.0 when the apparent 607 nm extinction is anomalously high, with intermediate values (1.3 to 2.0) lying between the two populations. This AOD ratio is used to select the suspect and control subsets examined in Fig. 4, but it is the $t > 3$ test that sets the archived flag.

Of the 397 nights tested, 105 (26 %) show detectable crosstalk (Fig. 4), concentrated in the spring and late-winter dust season (notably March 2022, November 2021, February 2024). On these nights, the 532 nm Raman extinction derived from the 607 nm channel is anomalously high, and the Ångström exponent (355/532 nm) is anomalously negative. A per-profile binary flag (leak607_crosstalk_flag) is included in the dataset. Users of the 607-channel-derived products (extinction at 532 nm, lidar ratio from the 607 path, Ångström exponent) should apply this flag. The 355 nm products (from the 387 nm Raman channel) are not affected by this artefact.

https://doi.org/10.5194/essd-2026-552
Preprint. Discussion started: 17 August 2026

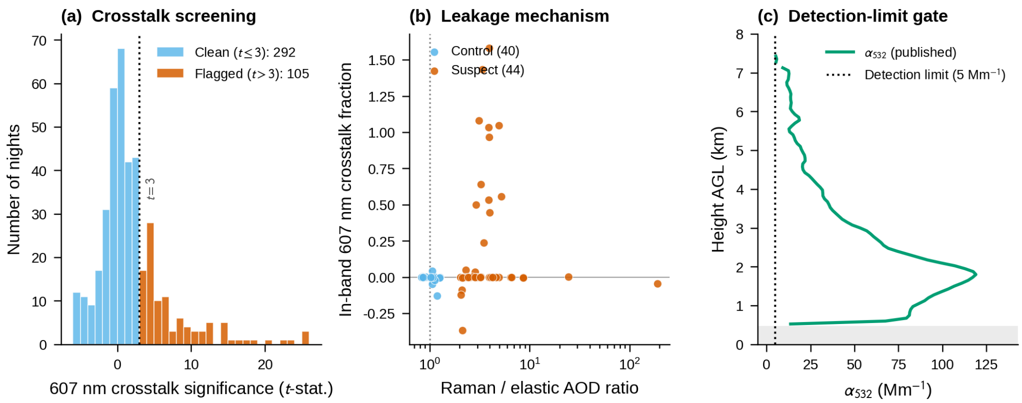

Figure 4. Quality control of the extinction product. (a) Screening for 532-into-607 nm elastic crosstalk in the 607 nm N_2-Raman channel: distribution of the crosstalk significance (t-statistic) over the 397 tested nights; 105 (26 %) exceed the t = 3 threshold and carry the leak607 flag in the dataset. (b) Leakage mechanism on the controlled subset (n = 84: 40 control and 44 suspect nights): the in-band crosstalk fraction rises with the Raman/elastic AOD ratio (logarithmic x-axis) for suspect nights, while control (clean) nights cluster near zero. (c) Extinction detection-limit gate (a representative high-coverage night): the published 532 nm extinction (green) is reported only where α > 5 Mm-1 (the absolute detection threshold ADET, dotted) and the relative uncertainty is below 50 %; below-threshold bins are withheld. The grey band marks the incomplete-overlap zone (< 0.45 km a.g.l.).

4.5 Depolarisation calibration epochs

As described in Sect. 3.5, the depolarisation calibration quality varies across three epochs. The dataset includes a per-night integer flag (depol_calibration) indicating the calibration method: 0 (uncalibrated, 64 nights in 2021), 1 (HV-gain LUT, 365 nights), or 2 (direct +/-45 degree, 8 nights). Users requiring quantitative depolarisation measurements should restrict their analysis to epochs 1 and 2, or exclude epoch 0 entirely. The ~85 % depolarisation availability quoted in Sect. 3.5 is 373 of the 437 nights and counts the 64 epoch-0 nights as uncalibrated.

5 Uncertainty budget

The dominant uncertainty source for each product is summarised in Table 2 and discussed by product in the subsections below.

Table 2. Uncertainty budget: dominant sources by product.

Source	Affected products	Magnitude	Type
Photon noise (Monte Carlo)	All	Median relative σ: 1.7 % (α 532), 0.5 % (β	Random, per-bin

https://doi.org/10.5194/essd-2026-552
Preprint. Discussion started: 17 August 2026

		532); P90 ~24 % at high altitudes	
Lidar-ratio assumption (S = 50 sr)	β 355/532, column AOD	+60 %/-18 % in AOD (S = 41/80 sr bounds)	Systematic, per-profile
Colour-ratio assumption (k = 1)	β 1064	Up to about 2x under strong dust (k = 0); about -30 percent for fine mode (k about 1.5)	Systematic
Depolarisation calibration	δ_v 532	Epoch 0 (64 nights): not released (_FillValue); Epoch 1 (HV-LUT, 365 nights): ~1.3 % (0.7 to 2.8 % per night; gain-law leave-one-out, σ_{V^*}/V^*), plus a residual receiver term ~+0.002 in δ_v (molecular-layer bound); Epoch 2 (Delta-90, direct): reference	Systematic, epoch-dependent
Water vapour calibration (C)	WVMR	~17 % (conservative upper bound; representativeness and SNR)	Systematic, constant
Overlap correction	Elastic backscatter near the surface (below the full-overlap height: 0.45 km at 532 nm, 0.68 km at 355 nm)	Corrected by the Raman overlap function (Sect. 4.2); bins with overlap below 0.5 set to _FillValue; residual a few percent just above the full-overlap height	Systematic
607 nm elastic crosstalk	α 532 (607 path), LR, Ångström	Variable; anomalously high α on flagged nights	Systematic, flagged nights

https://doi.org/10.5194/essd-2026-552
Preprint. Discussion started: 17 August 2026

Temperature/molecular-density profile	α 355/532 (Raman)	Small: a uniform T offset cancels in the log-derivative, only a lapse-rate error acts; estimated at most a few % (not separately propagated)	Systematic
Analogue/photon-counting gluing	All (2 to 5 km transition zone)	Not separately quantified; per-profile signal-dependent glue threshold	Systematic

5.1 Random uncertainty from photon noise

The statistical uncertainty from photon counting and analogue noise is propagated through the retrieval chain by Monte Carlo simulation. For each profile, the per-bin noise standard deviation (σ) is computed and archived. The median relative uncertainty (σ/value) is ~1.7 % for the extinction coefficient at 532 nm and ~0.5 % for the backscatter coefficient at 532 nm. At high altitudes (above ~8 km a.g.l.), where the signal is weaker, the relative uncertainty increases, with the 90th percentile reaching ~24 %. These statistics demonstrate that photon noise is not the precision-limiting factor for this dataset; the lidar-ratio systematic uncertainty dominates (Sect. 5.2).

5.2 Lidar-ratio systematic uncertainty

The elastic Fernald retrieval assumes a fixed lidar ratio of S = 50 sr. The true lidar ratio varies from night to night and within the column. The Raman-derived climatological lidar ratio is 51.6 sr (IQR 41 to 80 sr, n = 85 nights), with seasonal medians of 46 sr (DJF), 50 sr (MAM), 61 sr (JJA), and 51 sr (SON). The heavy upper tail (80 to 120 sr) reflects occasional strongly absorbing or mixed aerosol layers.

The sensitivity of the column AOD to the lidar-ratio assumption is characterised by first-order linear scaling: AOD(S) = AOD(50) × S/50 (Fig. 5). At S = 80 sr, the AOD increases by +60 %; at S = 41 sr, the AOD decreases by -18 % relative to the S = 50 baseline. These bounds are reported as per-profile variables in the dataset (column_aod_532_night_S41, column_aod_532_night_S80, and day equivalents). This is the dominant uncertainty: the precision of the aerosol optical properties in this dataset is limited by the lidar-ratio assumption, not by photon noise.

https://doi.org/10.5194/essd-2026-552
Preprint. Discussion started: 17 August 2026

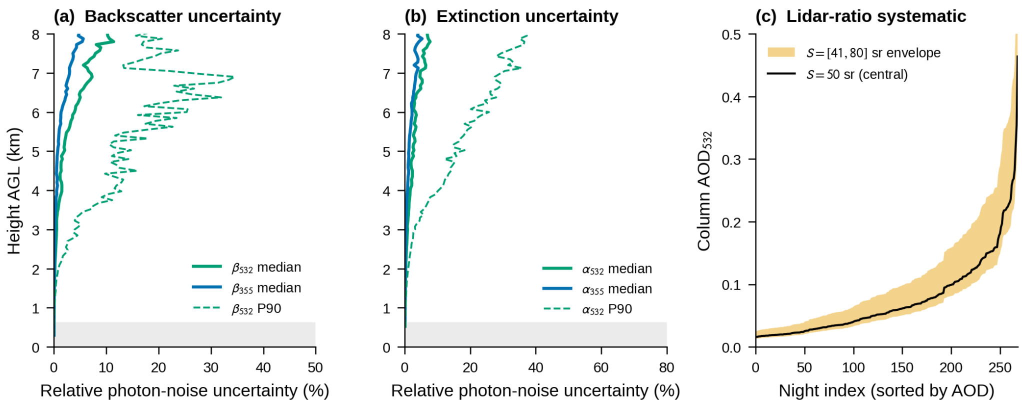

Figure 5. Uncertainty budget. (a) Per-bin relative photon-noise uncertainty (σ/value) profiles for α 532 (median 1.7 %, P90 ~24 %) and β 532 (median 0.5 %). (b) Lidar-ratio sensitivity: column AOD at S = 41 and S = 80 sr versus the baseline S = 50 sr, showing the first-order linear scaling with asymmetric +60 %/-18 % bounds (dashed lines).

5.3 Colour-ratio assumption

The 1064 nm backscatter product assumes a backscatter Ångström exponent k = 1. The actual exponent varies with aerosol type: near zero for coarse dust, above unity for fine-mode pollution. No independent constraint on k is available from this instrument. Because the transfer factor is 0.5 raised to the power k, the k = 1 assumption is accurate only to about a factor of two under strong dust (k = 0 gives twice the archived value) and to about -30 percent for fine-mode pollution (k about 1.5; Sect. 3.3); users should treat the 1064 nm backscatter as a non-independent, semi-quantitative colour-ratio estimate that can qualitatively indicate coarse- versus fine-mode dominance but should not be used for quantitative retrieval at 1064 nm.

5.4 Depolarisation and water-vapour calibration uncertainties

Two calibration constants carry systematic uncertainties. The depolarisation calibration varies by epoch, as detailed in Sect. 3.5: the 2021 nights (depol_calibration = 0) have no absolute calibration and are not released (set to _FillValue), the HV-LUT epoch (depol_calibration = 1) carries a ~1.3 % gain-law term (0.7 to 2.8 % per night; the relative gain-law prediction error $\sigma_{V*}/V*$ from leave-one-out cross-validation), plus a residual receiver term (diattenuation and finite beamsplitter extinction) bounded at about +0.002 in absolute δ_v from the molecular-layer check (Sect. 3.5), which dominates at low depolarisation (~10 % at δ_v ~ 0.02, below 2 % for dust), and the direct +/-45 degree nights (depol_calibration = 2) provide the reference. The water-vapour calibration constant C = 90.4 g kg^{-1} has a ~17 % uncertainty that propagates as a multiplicative bias on all WVMR values; it reflects both the Lhasa radiosonde spatial representativeness (the two sites are ~90 km apart) and the collocation signal-to-noise (Sect. 6.3), and is a conservative upper bound.

https://doi.org/10.5194/essd-2026-552
Preprint. Discussion started: 17 August 2026

5.5 Other systematic terms

Three further systematic terms are smaller than those above but are documented for completeness. First, the geometric overlap is corrected using the nitrogen-Raman overlap function (Sect. 4.2); the overlap reaches unity by 0.45 km (532 nm) and 0.68 km (355 nm), and the lowest bins where it falls below 0.5 are set to _FillValue, so no overlap-affected backscatter is reported. The residual uncertainty of the correction, estimated from the night-to-night spread of the overlap function, is at the level of a few percent immediately above the full-overlap height and is negligible over the free-tropospheric layer that carries most of the aerosol. Second, the Raman extinction uses the US Standard Atmosphere 1976 temperature profile scaled to surface pressure (Sect. 3.1); because the molecular number density enters the Raman inversion through the vertical gradient of its logarithm, a uniform temperature bias cancels and only an error in the temperature lapse rate acts, so substituting the local Lhasa radiosonde profile changes the retrieved extinction by at most a few percent, small relative to the lidar-ratio systematic and not separately propagated. Third, the analogue and photon-counting signals are joined by a per-profile, signal-dependent gluing threshold in the 2 to 5 km transition zone (Sect. 3.1); gluing errors can bias the profile shape locally in that zone, and this term is likewise not separately quantified. None of these three alters the conclusion that the lidar-ratio assumption dominates the optical-property uncertainty.

6 Dataset characterisation

6.1 Seasonal climatological profiles

The multi-year record permits a seasonal breakdown of the aerosol and water-vapour vertical structure (Fig. 6). We present the seasonal climatology using the products that are both physically reliable and well-sampled in the very clean plateau free troposphere (aerosol backscatter at 355 and 532 nm, the 532 nm volume depolarisation ratio, and the water-vapour mixing ratio), and we report in the same figure (panel e) the full-dataset per-height availability f(z) of each product. Seasonal medians are drawn only where at least 20 nights contribute at a given height. Per-night product availability over the 3.3-year record is high (backscatter 68 to 70 %, depolarisation 85 %, water vapour 99 %, extinction 98 %); the per-height coverage in panel (e) shows that the depolarisation and low-tropospheric water-vapour products are near-continuous, whereas aerosol backscatter is intermittent and layered, as expected for a pristine high-altitude site. The near-surface decline in aerosol-backscatter availability in panel (e) reflects the pristine nocturnal boundary layer rather than any loss of signal: on most nights the near-ground aerosol backscatter lies below the detection floor (0.5 Mm-1 sr-1) and is reported as _FillValue rather than as noise, so the availability rises with height towards the elevated layers where aerosol is more frequently detected. As a result, the seasonal backscatter medians reach the lowest ranges mainly in spring, the only season in which at least 20 nights carry detectable near-surface aerosol; in the cleaner summer, autumn and winter the near-ground medians are undefined and begin higher up.

https://doi.org/10.5194/essd-2026-552
Preprint. Discussion started: 17 August 2026

Aerosol backscatter is concentrated in the lowest ~2 to 3 km above the surface, with a warm-season elevated free-tropospheric layer. The seasonal loading is quantified most reliably by the validated column-AOD product rather than by any single profile: the seasonal column-AOD (532 nm) medians for detection nights are MAM 0.082, DJF 0.063, JJA 0.040 and SON 0.032. This is a pronounced spring (MAM) maximum driven by long-range-transported mineral dust and local sources, with an autumn (SON) minimum, consistent with the plateau dust climatology (Huang et al., 2007; Xu et al., 2020). The elevated spring and summer volume depolarisation is associated with coarse-mode dust, although the particle depolarisation is required to separate dust from ice (Sect. 6.2), and the summer water-vapour maximum (Sect. 6.3) reflects the Asian monsoon.

We deliberately do not show a seasonal-median Raman extinction profile. In the pristine free troposphere of the plateau the nighttime Raman extinction is detection-limited: it is retrievable on only 22 to 64 % of nights above 2 km, so an unconditional seasonal-median extinction profile would characterise a detection-censored, aerosol-loaded subset of nights rather than the typical state, and the paired 355/532 extinction Ångström is correspondingly unstable. Where the aerosol load is sufficient the Raman extinction is internally consistent, yielding a physically reasonable lidar ratio (layer S ≈ 41 sr, characteristic of dust; Fig. 3). The full extinction, lidar-ratio, depolarisation and particle-depolarisation profiles are therefore presented for that well-observed dust case study (like 8 December 2024).

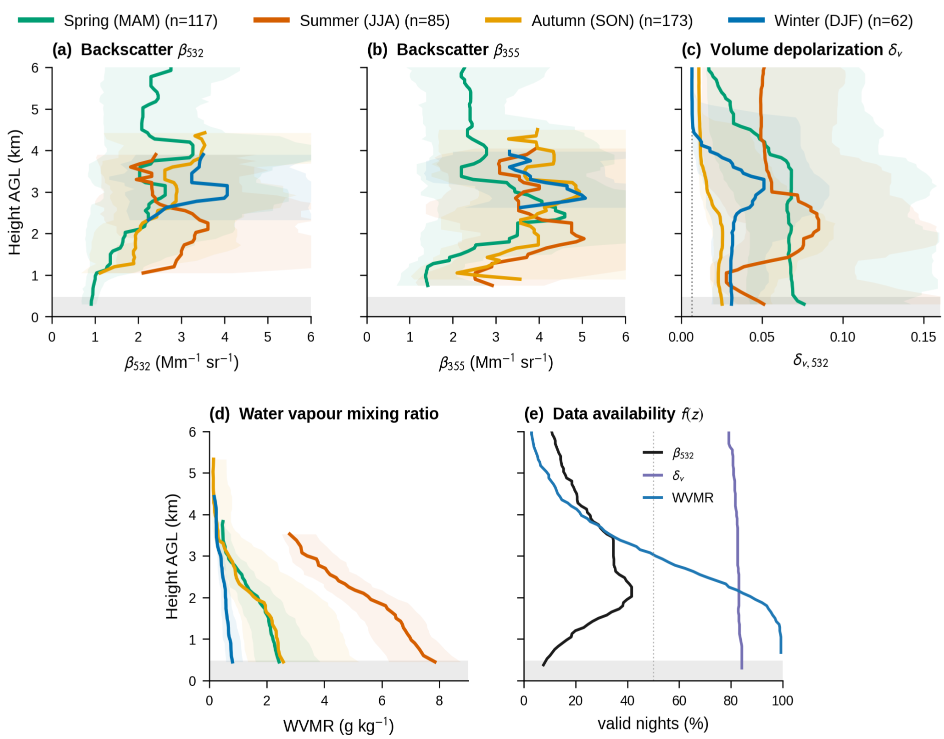

https://doi.org/10.5194/essd-2026-552
Preprint. Discussion started: 17 August 2026

Figure 6. Seasonal climatological profiles of the reliable multi-wavelength products for cloud-screened nights: (a) aerosol backscatter β_{532}, (b) β_{355}, (c) volume depolarisation $\delta_{v,532}$ (calibrated nights only; dotted line, molecular value), (d) water-vapour mixing ratio, and (e) full-dataset data availability f(z), the fraction of all 437 nights with a valid retrieval at each height, for β_{532}, δ_v and WVMR (dotted line, 50 %). Solid lines are seasonal medians; faint shading is the interquartile range. Medians are drawn only where at least 20 nights contribute at that height and are smoothed with a 0.5 km running median; the archived profiles are unsmoothed. The grey band marks the incomplete-overlap zone (< 0.45 km a.g.l.). Elastic backscatter is corrected for the geometric overlap (Sect. 4.2, Fig. S6).

6.2 Depolarisation and dust identification

The 532 nm depolarisation is the dataset's aerosol-type discriminant (Fig. 7). The 1 to 5 km layer-mean volume depolarisation ratio δ_v has a median of 0.047 over calibrated nights, with a long tail to high values. A high δ_v alone does not distinguish coarse mineral dust from ice, because both depolarise strongly; the two are separated by the particle linear depolarisation ratio δ_p (Sect. 3.5), which cannot exceed about 0.40 for mineral dust but reaches 0.45 to 0.8 for ice crystals. Classifying nights by a non-spherical layer (layer-mean $\delta_v > 0.10$) and then removing those with a confirmed ice layer ($\delta_p > 0.45$; Sect. 4.1) yields 61 dust nights and 141 near-spherical background nights ($\delta_v < 0.03$); a further 40 nights carry ice, and the remaining calibrated nights show intermediate layer-mean depolarisation (0.03 to 0.10) that is not assigned to a single aerosol type. Dust and background have distinct structure (Fig. 7b): dust nights carry an elevated non-spherical layer with a particle depolarisation of 0.19 (median; layer values ranging to about 0.40, characteristic of coarse mineral dust; Freudenthaler et al., 2009), whereas background nights are near-spherical throughout ($\delta_v \sim 0.01$ to 0.02). Dust occurrence is seasonal (Fig. 7c): 19 % of spring and 19 % of summer of the calibrated nights are dust, against 14 % in autumn and 13 % in winter. Because a high volume depolarisation can arise from either dust or ice, the volume-depolarisation product should be interpreted together with the archived particle depolarisation; neglecting the particle-depolarisation test would misclassify a substantial fraction of high-δ_v ice layers as dust.

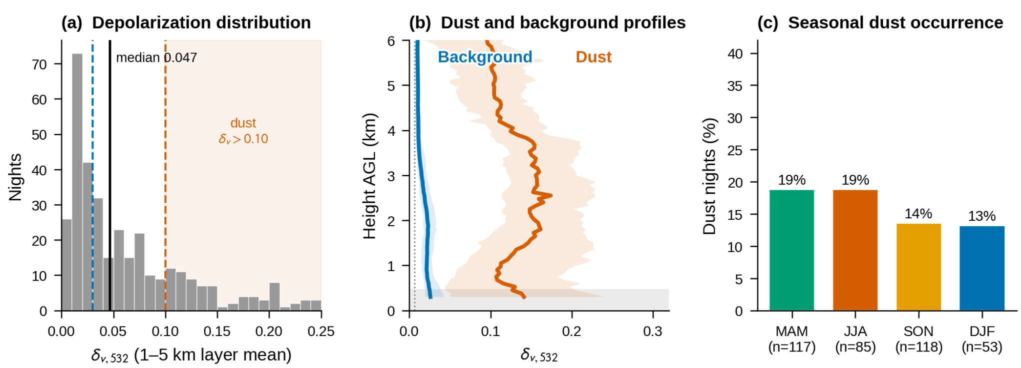

https://doi.org/10.5194/essd-2026-552
Preprint. Discussion started: 17 August 2026

Figure 7. Aerosol typing from the 532 nm volume depolarisation ratio (δv; calibrated nights only). (a) Distribution of the 1 to 5 km layer-mean δv (n = 369 calibrated nights; median 0.047; dashed lines mark the near-spherical background regime δv < 0.03 and the dust regime δv > 0.10, the latter shaded). (b) Composite median δv profiles with interquartile shading for dust nights (layer-mean δv > 0.10 with confirmed ice removed; n = 61) and background nights (δv < 0.03; n = 141); dotted line, molecular value. (c) Seasonal dust-occurrence frequency (fraction of calibrated nights classified as dust). The particle depolarisation ratio, which separates dust from ice, is archived and shown for a dust case in Fig. 3(g). The grey band marks the incomplete-overlap zone (< 0.45 km a.g.l.).

6.3 Water-vapour distribution and calibration

The WVMR product captures the extremely dry conditions at 4284 m a.s.l., with a surface-level median of 2.89 g kg^{-1} (range 0.17 to 12 g kg^{-1}). The seasonal cycle follows the monsoon moisture supply, summer (JJA) wettest and winter (DJF) driest (Fig. 6d), and in 98 % of profiles the WVMR decreases with altitude (negative overall gradient), consistent with the expected thermodynamic structure. The 408/387 nm Raman signal is calibrated against Lhasa radiosondes by a single transfer constant C = 90.4 g kg^{-1} (Fig. 8a). The high-SNR collocations, which best constrain the calibration, show no statistically significant temporal trend in C over the record (Theil-Sen 95 % confidence interval includes zero; p ~ 0.3), consistent with the use of a single constant; the weak apparent trend and the larger scatter in the full collocation set are associated with the low-SNR collocations, so we find no evidence for an instrument gain drift. The +/-17 % spread (median +/- MAD, n = 315 collocations) that defines the calibration uncertainty reflects both the lidar-radiosonde spatial representativeness (the two sites are ~90 km apart) and the collocation signal-to-noise: it narrows to 14 % for high-SNR collocations (versus 21 % for low-SNR), while the per-night internal spread is only 9 % (Fig. 8b).

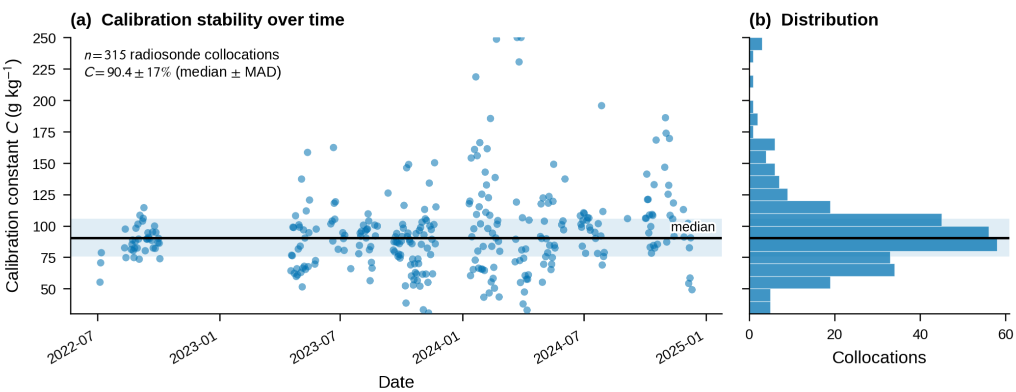

Figure 8. Radiosonde calibration and traceability of the water-vapour product (408/387 nm Raman). (a) Transfer constant C for every lidar-radiosonde collocation (n = 315; Lhasa, WMO 55591) versus date, with the median (90.4 g kg^{-1}, black line) and interquartile range (shaded). (b) Distribution of C (sharing the C axis): the +/-17 %

https://doi.org/10.5194/essd-2026-552
Preprint. Discussion started: 17 August 2026

spread (median +/- MAD) defining the calibration uncertainty, and the narrower spread for high-SNR collocations (14 %, versus 21 % for low-SNR). The seasonal WVMR climatology is shown in Fig. 6(d).

6.4 Ångström exponents

The extinction-related and backscatter-related Ångström exponents are computed from the 355/532 nm pair in bins where both wavelengths exceed their respective detection limits. In strong dust layers, the extinction Ångström exponent approaches ~0, consistent with coarse-mode dominance (physically expected for mineral dust). The site-residual Ångström exponent is approximately -0.05, which is within the method uncertainty and is not attributed to a physical mechanism. Users should be aware that the Ångström exponent is sensitive to the 607 nm crosstalk artefact (Sect. 4.4): on leak607-flagged nights, the 532 nm Raman extinction is anomalously high, driving the Ångström exponent anomalously negative. The leak607 flag should be applied before computing or interpreting Ångström exponents.

6.5 Sampling and column-AOD statistics

The dataset spans 40 months (September 2021 to December 2024), with 437 quality-controlled nights from 460 candidates. The observation frequency varies seasonally, with an autumn peak and a gap in January to May 2023 (instrument downtime; Fig. 9). The nighttime column AOD (532 nm) statistics are: detection-night median 0.053 (n = 269 of 437 nights), all-sample median 0.028; the remaining 168 nights (38 %) fall below the detection limit (upper-bound AOD ~0.016). Daytime column AOD (transmittance method) has a detection median of 0.078 (n = 208) and an all-sample median of 0.046. The daytime column AOD exceeds the nighttime value. Because the daytime and nighttime column AOD are retrieved by different methods (daytime transmittance versus nighttime Fernald and Raman inversion), part of this difference may be methodological; a physical contribution from daytime convective lofting is plausible but is not established here.

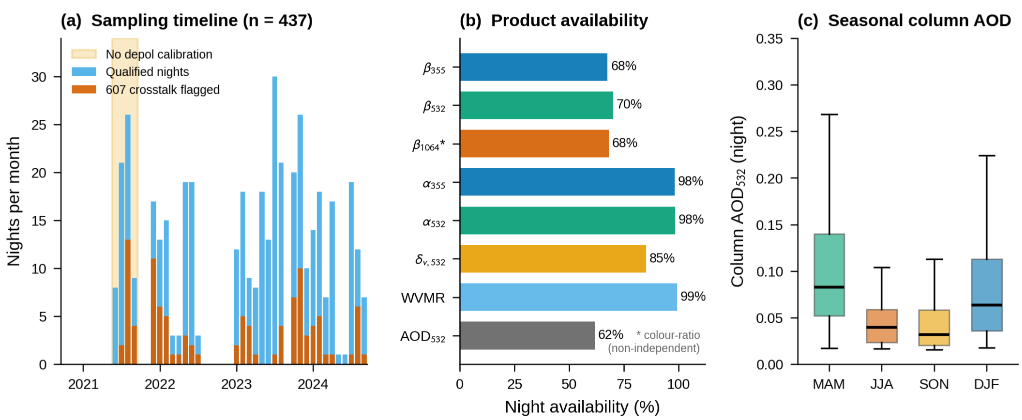

https://doi.org/10.5194/essd-2026-552
Preprint. Discussion started: 17 August 2026

Figure 9. Data overview. (a) Monthly profile count (night) across the 2021 to 2024 period (n = 437), showing qualified nights, the 607 nm crosstalk-flagged nights, the uncalibrated-depolarisation 2021 epoch (shaded), and the January to May 2023 instrument-downtime gap. (b) Per-product per-night availability (%) across all 437 nights: backscatter 355 (68 %), backscatter 532 (70 %), backscatter 1064 (68 %, colour-ratio, non-independent), extinction 355 and 532 (98 %), depolarisation (85 %), WVMR (99 %), and column AOD (62 %). (c) Seasonal nighttime column AOD at 532 nm (boxplots: MAM, JJA, SON, DJF).

7 Independent corroboration

The term "corroboration" is used deliberately rather than "validation," because the comparisons presented here do not constitute a point-for-point validation of the profile products. They demonstrate consistency at the column and climatological level.

7.1 Column AOD against AERONET at Nam Co

The AERONET Version 3 Level 2.0 sun photometer at Nam Co (30.77° N, 90.96° E, 4746 m a.s.l.; Giles et al., 2019) is located ~85 km northeast of Yangbajing. AERONET AOD at 440 and 675 nm is interpolated to 532 nm using the measured 440/675 nm Ångström exponent: $AOD(532) = AOD(440) \times (532/440)^{(-AE\_440\text{-}675)}$. Daytime lidar column AOD is compared with near-overpass AERONET AOD (UTC 06:00 to 09:00) for 41 same-day pairs (Fig. 10). The results are: median bias (Yangbajing minus AERONET) +0.005, RMSE 0.179, Pearson $r = 0.61$ ($p < 0.001$), Spearman rank correlation 0.72 ($p < 0.001$), AERONET median AOD 0.037 (n = 189 days), lidar daytime detection median AOD 0.078 (n = 208). The per-pair scatter is large, reflecting the ~85 km spatial separation, the ~460 m higher elevation of Nam Co (4746 m), whose column lies above the lowest part of the Yangbajing aerosol layer, the lakeside setting of Nam Co, which may sample a somewhat cleaner air mass, and the differing sampling volumes (point column vs. sun-photometer cone). These differences plausibly contribute to the lower full-sample AERONET median, whereas the matched-pair median bias is near zero (+0.005). Because the per-pair RMSE (0.179) exceeds the median AOD itself, the primary result is the significant rank-order correlation ($\rho = 0.72$) and the agreement of the two climatological medians, not per-pair agreement; the near-zero median bias should therefore be read as consistency of the distributions rather than as point-for-point validation. The AERONET median (0.037) and the lidar daytime all-sample median (0.046) are of the same order, consistent with both instruments observing the same clean, high-altitude aerosol regime.

https://doi.org/10.5194/essd-2026-552
Preprint. Discussion started: 17 August 2026

Open Access Earth System Science Data Discussions

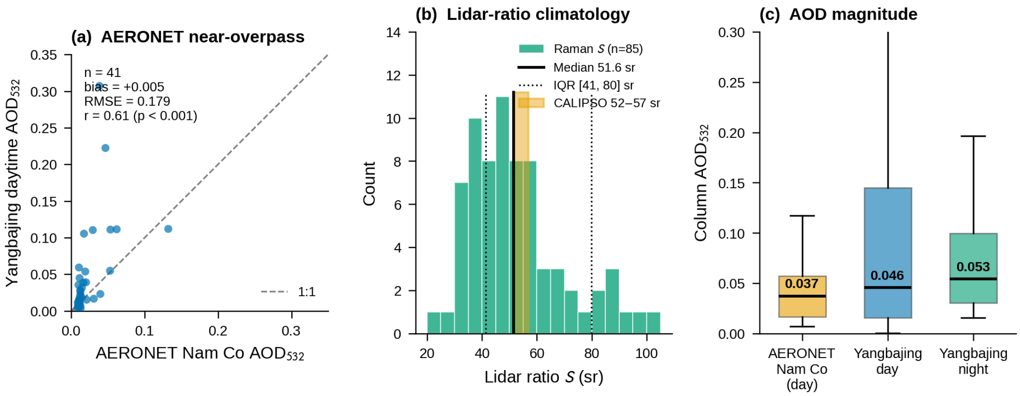

Figure 10. Independent corroboration against AERONET Nam Co. (a) Same-day near-overpass (UTC 06:00 to 09:00) scatter plot (n = 41) of daytime lidar column AOD (532 nm) vs. AERONET AOD (440/675 nm interpolated to 532 nm), with 1:1 line, median bias (+0.005), r (0.61; p < 0.001), and RMSE (0.179) annotated. (b) Probability density functions of daytime AOD for the lidar (n = 208 detection days, median 0.078) and AERONET (n = 189, median 0.037). (c) Nighttime AOD distribution (n = 269 detection nights, median 0.053).

7.2 Lidar ratio and column AOD against CALIPSO

The independent lidar-ratio constraint here is the Raman-derived site-mean of 51.6 sr, which agrees with the CALIPSO Version 4 "clean continental" lidar ratio for this region, 51.7 to 56.9 sr (count- to optical-depth-weighted over 548 layers; Kim et al., 2018). Because the CALIOP operational lidar ratio is a type-selected model prior rather than a retrieval for these tenuous layers, this agreement corroborates the Raman value against CALIPSO's assumed climatology, not against an independent CALIOP measurement. The CALIOP column AOD over the site, by contrast, is far lower than the ground value on the 46 coincident nighttime overpasses (CALIOP median 0.003 versus a ground median of about 0.05, the lidar nighttime detection-night column AOD on the same nights), consistent with CALIOP's known low sensitivity to tenuous aerosol over bright, high terrain (Kim et al., 2017; Toth et al., 2018). The CALIPSO comparison therefore corroborates the lidar-ratio assumption and the aerosol type; a column-AOD comparison reflects the satellite's detection sensitivity rather than a discrepancy in the ground data, and does not constitute a profile-level validation.

7.3 Water-vapour calibration against Lhasa radiosondes

The WVMR calibration constant ($C = 90.4\ g\ kg^{-1}$) is determined by regression against Lhasa radiosondes (n = 315 nights). The ~17 % uncertainty reflects both the ~90 km spatial representativeness between the two sites and the collocation signal-to-noise (Sect. 6.3). This is a calibration transfer, not an independent validation: the radiosonde is used to set the calibration constant, so agreement is by construction. Independent

https://doi.org/10.5194/essd-2026-552
Preprint. Discussion started: 17 August 2026

validation of the WVMR product against a co-located reference (e.g. a co-sited radiosonde) is not available at this time and represents an opportunity for future work.

8 Dataset description

8.1 File and format

The dataset is archived as a single CF NetCDF-4 file: Yangbajing_lidar_multiwavelength_2021-2024.nc The file contains 36 variables on the common 75 m vertical grid (157 levels; dimensions: night = 437, altitude = 157, day = 279), including two ancillary variables (overlap_355, overlap_532) that store the nitrogen-Raman geometric overlap functions applied in the near-field correction (Sect. 4.2). All floating-point variables carry _FillValue = -999.0 and long_name attributes. Several variables also carry a CF standard_name: extinction (volume_extinction_coefficient_in_air_due_to_ambient_aerosol_particles), water-vapour mixing ratio (humidity_mixing_ratio), column AOD (atmosphere_optical_thickness_due_to_ambient_aerosol_particles), altitude (height), and latitude/longitude; the aerosol backscatter carries a long_name only, as CF has no standard name for the particulate backscatter coefficient. Extinction variables carry units = "m^{-1}" and column-AOD variables units = "1". Time coordinates use units = "days since 2021-01-01 00:00:00" with calendar = "standard". The quality and cloud flags carry flag_values and flag_meanings rather than a physical unit. All units strings are UDUNITS-2-compatible.

8.2 Archived variables and quality flags

Table 3. Dataset variables. Dimensions: night = 437, altitude = 157, day = 279.

Variable	Dimensions	Units	Method	Availability	Maturity
altitude	(altitude)	m a.g.l.	Grid coordinate	157 levels	n/a
night_time	(night)	days since 2021-01-01	Temporal coordinate	437	n/a
day_time	(day)	days since 2021-01-01	Temporal coordinate	279	n/a
latitude	scalar	degrees_north	Fixed station coordinate (30.102)	n/a	n/a
longitude	scalar	degrees_east	Fixed station coordinate (90.522)	n/a	n/a

https://doi.org/10.5194/essd-2026-552
Preprint. Discussion started: 17 August 2026

Open Access Earth System Science Data Discussions

backscatter_355	(night, altitude)	m^{-1} sr^{-1}	Elastic Fernald, S = 50	~68 %	A
backscatter_532	(night, altitude)	m^{-1} sr^{-1}	Elastic Fernald, S = 50	~70 %	A
backscatter_1064	(night, altitude)	m^{-1} sr^{-1}	Colour-ratio transfer (k = 1)	~68 to 70 %	B
extinction_355	(night, altitude)	m^{-1}	Raman 387 nm, derivative	~98 %	A
extinction_532	(night, altitude)	m^{-1}	Raman 607 nm, derivative	~98 %	A
volume_depolarization_532	(night, altitude)	1	Cross/parallel ratio, calibrated	~85 %	B
particle_depolarization_532	(night, altitude)	1	From δ_v and R (dm = 0.0065); R >= 2.5 only	detected R >= 2.5 bins	B
water_vapour_mixing_ratio	(night, altitude)	g kg^{-1}	408/387 ratio, C = 90.4	~99 %	B
angstrom_extinction	(night, altitude)	1	355/532 extinction pair	dual-detect bins	B
angstrom_backscatter	(night, altitude)	1	355/532 backscatter pair	dual-detect bins	B
column_aod_532_night	(night)	1	Integrated extinction	n = 269 detect	A
column_aod_532_night_qc	(night)	flag	AOD quality flag	all	A
column_aod_532_night_S41	(night)	1	LR sensitivity bound (S = 41)	as above	A
column_aod_532_night_S80	(night)	1	LR sensitivity bound (S = 80)	as above	A
column_aod_532_day	(day)	1	Transmittance ratio	n = 208 detect	A
column_aod_532_day_qc	(day)	flag	AOD quality flag	all	A
column_aod_532_day_S41	(day)	1	LR sensitivity bound (S = 41)	as above	A
column_aod_532_day_S80	(day)	1	LR sensitivity bound (S = 80)	as above	A

https://doi.org/10.5194/essd-2026-552
Preprint. Discussion started: 17 August 2026

Open Access Earth System Science Data Discussions

sigma_backscatter_355	(night, altitude)	m^{-1} sr^{-1}	Photon-noise std. dev.	as backscatter_355	A
sigma_backscatter_532	(night, altitude)	m^{-1} sr^{-1}	Photon-noise std. dev.	as backscatter_532	A
sigma_extinction_355	(night, altitude)	m^{-1}	Photon-noise std. dev.	as extinction_355	A
sigma_extinction_532	(night, altitude)	m^{-1}	Photon-noise std. dev.	as extinction_532	A
depol_calibration	(night)	flag (0/1/2)	Calibration epoch	all	A
leak607_crosstalk_flag	(night)	flag (0/1)	607 elastic leakage test	all	A
cloud_free_night	(night)	flag (0/1)	Scattering-ratio cloud screen, A-refined (Sect. 4.1)	all	A
cloud_detected	(night)	flag (0/1)	Any cloud layer detected (R>10 or cirrus gate)	all	A
cloud_base_km	(night)	km	Lowest detected cloud-base height a.g.l.	detected nights	A
cloud_top_km	(night)	km	Highest detected cloud-top height a.g.l.	detected nights	A
cloud_phase	(night)	flag (0/1/2/3)	Cloud phase: none/water/ice/undetermined	all	B
overlap_532	(altitude)	1	Raman overlap (Wandinger & Ansmann, 2002)	–	A
overlap_355	(altitude)	1	Raman overlap (Wandinger & Ansmann, 2002)	–	A

Maturity levels: A = mature, quality-controlled; B = limited (known caveats, see Sect. 3 and 9). Experimental products are not included in the archive.

https://doi.org/10.5194/essd-2026-552
Preprint. Discussion started: 17 August 2026

Missing values are indicated by _FillValue = -999. Extinction is reported in SI units (m^{-1}). Typical aerosol extinction values at this site are of order 10^{-6} to 10^{-4} m^{-1}, equivalent to 1 to 100 Mm^{-1}, the unit used in the figures.

8.3 Spatial and temporal coverage

The archive contains 437 nighttime profiles and 279 daytime column-AOD retrievals spanning September 2021 to December 2024; the nighttime profiles are on the common vertical grid of 157 levels from 0.30 to 12 km a.g.l. (approximately 4584 to 16284 m a.s.l.) at 75 m spacing, with an effective vertical resolution that is altitude-dependent and coarser than the grid for extinction (Sect. 3.4) and about 75 m for backscatter. The archived quantities are the three backscatter coefficients (355, 532, 1064 nm), the two Raman extinction coefficients (355, 532 nm), the 532 nm volume depolarisation ratio, the water-vapour mixing ratio, the Ångström exponents, and the night and day column AOD with their quality flags and lidar-ratio-sensitivity bounds, together with the per-bin uncertainty fields and quality flags (Table 3).

8.4 Global attributes

The NetCDF file includes CF global attributes: Conventions = "CF-1.8", title, summary, institution, history, references, molecular_profile = "US Standard Atmosphere 1976 T(z) scaled to measured surface pressure", uncertainty_note, vertical_caliber_note, and license = "Creative Commons Attribution 4.0 International (CC-BY-4.0)". Floating-point variables carry _FillValue, long_name, and where applicable units and standard_name. The flag variables (cloud_free_night, cloud_detected, cloud_phase, depol_calibration, leak607_crosstalk_flag) are integer-type with flag_values and flag_meanings attributes. The global attribute cloud_screening_note documents the scattering-ratio cloud screen (Sect. 4.1). All units strings are UDUNITS-2-compatible, and the file conforms to the CF-1.8 conventions; the retrieved aerosol backscatter carries a long_name only, as CF has no standard name for the particulate backscatter coefficient.

9 Usage notes and caveats

Several limitations govern how the dataset should be used, most of them tied to the vertical range over which each product is reliable. The full multi-wavelength capability is available only in the nighttime free troposphere. Reliable retrievals begin at the full-overlap height, 0.45 km a.g.l. at 532 nm and 0.68 km at 355 nm (about 4.7 to 5.0 km a.s.l.), below which the geometric overlap is incomplete and the Raman signal is too weak for an independent extinction retrieval; the products in this near-field zone rely on the elastic Fernald inversion with an assumed lidar ratio of 50 sr, aerosol below it is not captured, and the column AOD is therefore a lower bound. The 1064 nm backscatter is a non-independent colour-ratio transfer (Sect. 3.3) rather than an independent measurement. The practical vertical caliber is thus an independent two-wavelength Raman extinction at night in the free troposphere, an elastic two-wavelength backscatter (355 and 532 nm)

https://doi.org/10.5194/essd-2026-552
Preprint. Discussion started: 17 August 2026

with an assumed lidar ratio, a non-independent 1064 nm colour ratio, the volume depolarisation ratio, and the water-vapour mixing ratio; it is not a fully independent "three-backscatter plus two-extinction" product in the EARLINET sense. The grid spacing is 75 m, but the effective vertical resolution is coarser for the Raman extinction, altitude-dependent and increasing with height (a few hundred metres in the lower free troposphere to of order 1 km aloft; Sect. 3.4), while for backscatter it is close to the grid spacing; comparisons with other datasets should use the effective resolution.

The lidar-ratio assumption is the dominant source of uncertainty and is accompanied by two epoch-specific calibration caveats. All elastic backscatter and column AOD values assume S = 50 sr, whereas the true lidar ratio varies over roughly a factor of two (climatological IQR 41 to 80 sr); scaling the AOD to the S = 41 and 80 sr bounds gives an asymmetric envelope of +60 %/-18 %, and the per-profile S41 and S80 AOD bounds are provided in the dataset (Table 3). For the depolarisation product, the 2021 epoch (64 nights) lacks an absolute calibration and should be excluded from quantitative use, while the HV-LUT epoch (365 nights) carries a gain-law calibration term of about 1.3 % (0.7 to 2.8 % per night; the relative gain-law prediction error $\sigma_{V*}/V*$ from leave-one-out cross-validation), plus a residual receiver term (diattenuation and finite beamsplitter extinction) bounded at about +0.002 in absolute δ_v from the molecular-layer check, which dominates at low depolarisation (~10 % at δ_v ~ 0.02, below 2 % for dust; Sect. 3.5). The water-vapour calibration constant C = 90.4 g kg^{-1} has an uncertainty of about 17 %, a conservative upper bound reflecting the radiosonde spatial representativeness (~90 km) and the collocation signal-to-noise, and no co-located independent water-vapour reference is available for validation.

Users of the 607 nm nitrogen-Raman channel must additionally apply the crosstalk flag. On 105 of the 397 nights with an operational 607 nm channel (26 %) this channel is contaminated by elastic leakage from the strong 532 nm return (Sect. 4.4), and the leak607_crosstalk_flag should be applied before using any 607-derived product, namely the 532 nm extinction, the lidar ratio, and the extinction Ångström exponent.

Within these bounds the dataset supports a range of applications: the evaluation of spaceborne lidar detection over clean high-altitude terrain, ground-truth benchmarking of reanalysis and model aerosol profiles, aerosol-type classification from the depolarisation and Ångström exponents, water-vapour profiling in the upper troposphere, and, for well-observed cases such as dust events, input to radiative-transfer calculations. Users should cite both this paper and the Zenodo dataset DOI.

10 Discussion

10.1 Independence boundary and benchmarking against EARLINET

The instrument is configured like an EARLINET "3 + 2" multi-wavelength Raman lidar (Baars et al., 2016), with elastic and nitrogen-Raman channels at 355/387 and 532/607 nm and an elastic channel at 1064 nm, so it is in principle capable of an independent three-backscatter, two-extinction retrieval. In this dataset the

https://doi.org/10.5194/essd-2026-552
Preprint. Discussion started: 17 August 2026

Open Access Earth System Science Data Discussions

independent products are the nitrogen-Raman extinction (Ansmann et al., 1990) at 355 and 532 nm and the Raman-derived lidar ratio; the aerosol backscatter at 355 and 532 nm is the elastic (Fernald) product under an assumed lidar ratio, and the 1064 nm backscatter is a non-independent colour-ratio transfer (Sect. 3.3). We tested whether the assumption could be removed by applying the self-calibrated elastic/Raman backscatter method (Ansmann et al., 1992) across the record. Over the highest-quality nights (adequate signal, cloud-free, 607 nm return above 4 km; n = 122) the self-calibrated Raman backscatter agrees with the archived elastic backscatter within 30 % on fewer than one night in five (18 %); the ratio of the two has a median of 1.48 but an interquartile range of 0.79 to 2.27, that is a factor-of-three spread. The lidar ratio derived from the self-calibrated backscatter spans two orders of magnitude and is physically plausible on only about 60 % of nights under a generous 15 to 100 sr window, falling to about 50 % under a stricter 20 to 90 sr window (Fig. S5). This is the documented behaviour of the Raman backscatter method in clean air, not an instrumental fault. The reason is mechanistic: the aerosol backscatter is recovered as a small perturbation on the molecular signal from an inelastic return roughly 103 times fainter than the elastic one, and its calibration against an aerosol-free reference is where the low-signal noise enters, whereas the extinction is a log-signal derivative that needs no such faint-perturbation normalisation and is comparatively robust (Mattis et al., 2004; Pappalardo et al., 2004). Consistent with this, the retrieval reproduces the elastic backscatter when the aerosol signal is adequate, matching the 8 December 2024 dust case to within 11 % (a high-signal best case), and the two forms of the Raman extinction, the derivative slope and the derivative-free transmittance, agree to a median of 5 %. We therefore archive the elastic backscatter with a fixed S = 50 sr, a value that the Raman lidar ratio corroborates in the median (51.6 sr, interquartile range 41 to 80 sr; the CALIPSO Version 4 clean-continental prior is 51.7 to 56.9 sr). We release the Raman lidar ratio and the per-profile S = 41 and 80 sr AOD bounds so that the assumption can be propagated. Separating an assumed-lidar-ratio backscatter product from an independent extinction and lidar-ratio product is the design of the EARLINET Single Calculus Chain (D'Amico et al., 2015; Mattis et al., 2016); it is the appropriate treatment of a low-aerosol site, and we state it plainly so that the dataset is not taken for a fully independent three-backscatter, two-extinction record.

10.2 The lidar-ratio assumption in quantitative use

The fixed lidar ratio, not photon noise, is the dominant uncertainty (Sect. 5.2): scaling to the S = 41 and 80 sr bounds changes the column AOD by +60 %/-18 %. Because a single value is applied at all heights, it cannot follow genuine layer-to-layer changes in aerosol type, so the assumption affects the shape as well as the magnitude of the backscatter and AOD profiles. Quantitative applications of the backscatter and AOD should use the per-profile bounds provided with the data, whereas the nighttime free-tropospheric extinction and lidar ratio, which do not depend on the assumption, are the appropriate products for quantitative optical work.

https://doi.org/10.5194/essd-2026-552
Preprint. Discussion started: 17 August 2026

10.3 Cloud screening near the surface

The dense-cloud gate (scattering ratio R > 10) is an empirical, site-derived threshold rather than a first-principles value: the peak-layer scattering ratio of aerosol layers reaches at most 10.0 over the whole record (95th percentile 8.9), whereas dense clouds begin at R ≈ 10.6 (fifth percentile), and thin cold cirrus below this value is captured instead by the coincident depolarisation and temperature criterion and the particle-depolarisation ice gate (Sect. 4.1), following the scattering-ratio, depolarisation and temperature feature space of the CALIPSO cloud-aerosol discrimination scheme. Near the surface the separation is intrinsically more difficult, because fog, low stratus and blowing dust can produce comparable scattering ratios; we did not carry out a dedicated near-surface sensitivity test, so users working in the lowest ~2 km should treat the cloud flags there conservatively and use the archived cloud-base and thermodynamic-phase information rather than a single threshold.

10.4 Applications and outlook

The dataset provides the vertically resolved aerosol ground reference that the plateau interior has lacked. Its most direct application is the evaluation of spaceborne lidar over clean, high-albedo terrain: on the 46 coincident nighttime CALIPSO overpasses the CALIOP column AOD is far below the coincident ground value (CALIOP median 0.003 against a ground median of about 0.05, the lidar nighttime column AOD on the same nights), a quantitative illustration of the satellite's detection floor over the bright, high plateau that the ground record can help characterise, both for CALIPSO and for the forthcoming EarthCARE/ATLID high-spectral-resolution lidar (Illingworth et al., 2015; Wandinger et al., 2023). The depolarisation and particle-depolarisation products support aerosol typing and the separation of mineral dust from ice; the extinction and lidar ratio constrain reanalysis and model aerosol profiles; and the well-observed dust cases (Fig. 3) supply vertically resolved input for radiative-transfer calculations. A co-sited radiosonde, or a reference sun photometer at the lidar itself, would remove the main residual uncertainties in the water-vapour and AOD products and is the natural next step.

11 Conclusions

This paper documents what is, to our knowledge, the first openly archived, multi-year ground-based multi-wavelength aerosol profile dataset from the clean interior of the Tibetan Plateau. The dataset (Yangbajing, 4284 m a.s.l., September 2021 to December 2024) provides 437 nighttime profiles and 279 daytime column-AOD retrievals, with aerosol backscatter (355, 532, 1064 nm), Raman extinction (355, 532 nm), volume and particle depolarisation (532 nm), water vapour mixing ratio (408/387 nm), Ångström exponents, column AOD, per-bin photon-noise uncertainty, and quality flags, all on a 75 m vertical grid (157 levels). No station of the EARLINET, MPLNET, or AD-Net lidar networks operates in this region (public station lists reviewed June 2026), and the dataset fills a gap in the vertical aerosol observational record over the Third Pole (Table 4).

Table 4. Comparison of this dataset with existing ground-based lidar networks/datasets over and near the Tibetan Plateau.

Network/Dataset	Location	Interior TP?	Duration	Products	Open archive?
This work	Yangbajing (30.1° N, 90.5° E, 4284 m)	Yes (>100 km from edge)	2021–2024 (3.3 yr)	2 β + 1 colour-ratio β + 2 α + δ_v + WVMR	Yes (Zenodo, CC-BY-4.0)
MPLNET	Various; nearest TP-relevant: none interior	No	Varies	1 β (532)	Yes
AD-Net	East Asia; nearest: none interior TP	No	Varies	1 to 2 β	Yes
NDACC	Global; no interior TP station	No	Varies	Multi-wavelength (varies)	Yes
EARLINET/ACTRIS	Europe	No	2000 to present	3 β + 2 α (at reference stations)	Yes
Baars et al. (2016)	PollyNET, global	No interior TP	2013 to 2016	3 β + 2 α + δ_v	Yes

The principal caveat for quantitative use is the lidar-ratio assumption that underlies the elastic backscatter and the column AOD (Sect. 10.1, 10.2); the independent nitrogen-Raman extinction and lidar ratio, the depolarisation, and the water vapour mixing ratio are the products intended for quantitative work in the nighttime free troposphere, each with the per-bin uncertainty and quality flags needed to use it correctly. By openly archiving a multi-year, quality-controlled, multi-wavelength record from the cleanest part of the Third Pole, the dataset supplies the vertical aerosol ground truth that spaceborne-lidar evaluation, reanalysis and model assessment, and radiative studies over the plateau have until now had to do without.

Data availability

The archived products are Level 2. The dataset is archived on Zenodo as a single CF-1.8 NetCDF-4 file, Yangbajing_lidar_multiwavelength_2021-2024.nc, under the CC-BY-4.0 license (Wang et al., 2026; https://doi.org/10.5281/zenodo.21317571). The record is openly and anonymously available to editors, reviewers, and the public through the registered DOI, without login or access restriction.

Third-party data used for corroboration are not redistributed here. The CALIPSO Level-2 5 km aerosol profile product (Version 4-51; NASA/LARC/SD/ASDC, 2018) is available from the NASA Langley Atmospheric Science Data Center Distributed Active Archive Center (https://doi.org/10.5067/CALIOP/CALIPSO/CAL_LID_L2_05kmAPro-Standard-V4-51); the AERONET Version 3 Level 2.0 data for Nam Co from https://aeronet.gsfc.nasa.gov (Giles et al., 2019); and the Lhasa radiosonde data (WMO 55591) from the IGRA2 archive (https://www.ncei.noaa.gov/products/weather-balloon/integrated-global-radiosonde-archive).

Author contributions

YW designed and operated the lidar system, developed the retrieval and quality-control code, produced the dataset, wrote the manuscript, and supervised the project together with DL. HC contributed to the data analysis and quality control. WZ contributed to the cloud screening and data quality control. YBi contributed to instrument maintenance and field operations. TW contributed to field operations and data processing. DL provided the observational infrastructure and station support and supervised the project.

Competing interests

The authors declare that they have no conflict of interest.

Acknowledgements

The authors thank the staff of the Yangbajing Whole-Atmosphere Observatory for their support in maintaining the lidar system.

Financial support

This work is supported by the Strategic Priority Research Program of Chinese Academy of Sciences, Grant No. XDA0470301, Jing-Jin-Ji Regional Integrated Environmental Improvement-National Science and Technology Major Project (No. 2025ZD1204800) and Brazil Convection and Whole-Atmosphere Coupling Project (Grant No. 119GJHZ2025054MI). We acknowledge the use of lidar data from the Chinese Meridian Project.

References

Ansmann, A., Riebesell, M., and Weitkamp, C.: Measurement of atmospheric aerosol extinction profiles with a Raman lidar, Opt. Lett., 15, 746–748, https://doi.org/10.1364/OL.15.000746, 1990.

https://doi.org/10.5194/essd-2026-552
Preprint. Discussion started: 17 August 2026

Ansmann, A., Riebesell, M., Wandinger, U., Weitkamp, C., Voss, E., Lahmann, W., and Michaelis, W.: Independent measurement of extinction and backscatter profiles in cirrus clouds by using a combined Raman elastic-backscatter lidar, Appl. Optics, 31, 7113–7131, https://doi.org/10.1364/AO.31.007113, 1992.

Baars, H., Kanitz, T., Engelmann, R., Althausen, D., Heese, B., Komppula, M., Preissler, J., Tesche, M., Ansmann, A., Wandinger, U., Lim, J.-H., Ahn, J. Y., Stachlewska, I. S., Amiridis, V., Marinou, E., Seifert, P., Hofer, J., Skupin, A., Schneider, F., Bohlmann, S., Foth, A., Bley, S., Pfuller, A., Giannakaki, E., Lihavainen, H., Viisanen, Y., Hooda, R. K., Pereira, S. N., Bortoli, D., Wagner, F., Mattis, I., Janicka, L., Markowicz, K. M., Achtert, P., Artaxo, P., Pauliquevis, T., Souza, R. A. F., Sharma, V. P., van Zyl, P. G., Beukes, J. P., Sun, J., Rohwer, E. G., Deng, R., Mamouri, R.-E., and Zamorano, F.: An overview of the first decade of PollyNET: an emerging network of automated Raman-polarization lidars for continuous aerosol profiling, Atmos. Chem. Phys., 16, 5111–5137, https://doi.org/10.5194/acp-16-5111-2016, 2016.

Behrendt, A. and Nakamura, T.: Calculation of the calibration constant of polarization lidar and its dependency on atmospheric temperature, Opt. Express, 10, 805–817, https://doi.org/10.1364/OE.10.000805, 2002.

Comeron, A., Munoz-Porcar, C., Rodriguez-Gomez, A., Sicard, M., Dios, F., Gil-Diaz, C., dos Santos Oliveira, D. C. F., and Rocadenbosch, F.: An explicit formulation for the retrieval of the overlap function in an elastic and Raman aerosol lidar, Atmos. Meas. Tech., 16, 3015–3025, https://doi.org/10.5194/amt-16-3015-2023, 2023.

D'Amico, G., Amodeo, A., Baars, H., Binietoglou, I., Freudenthaler, V., Mattis, I., Wandinger, U., and Pappalardo, G.: EARLINET Single Calculus Chain, overview on methodology and strategy, Atmos. Meas. Tech., 8, 4891–4916, https://doi.org/10.5194/amt-8-4891-2015, 2015.

Fernald, F. G.: Analysis of atmospheric lidar observations: some comments, Appl. Optics, 23, 652–653, https://doi.org/10.1364/AO.23.000652, 1984.

Freudenthaler, V., Esselborn, M., Wiegner, M., Heese, B., Tesche, M., Ansmann, A., Muller, D., Althausen, D., Wirth, M., Fix, A., Ehret, G., Knippertz, P., Toledano, C., Gasteiger, J., Garhammer, M., and Seefeldner, M.: Depolarization ratio profiling at several wavelengths in pure Saharan dust during SAMUM 2006, Tellus B, 61, 165–179, https://doi.org/10.1111/j.1600-0889.2008.00396.x, 2009.

Freudenthaler, V.: About the effects of polarising optics on lidar signals and the Delta-90 calibration, Atmos. Meas. Tech., 9, 4181–4255, https://doi.org/10.5194/amt-9-4181-2016, 2016.

Giles, D. M., Sinyuk, A., Sorokin, M. G., Schafer, J. S., Smirnov, A., Slutsker, I., Eck, T. F., Holben, B. N., Lewis, J. R., Campbell, J. R., Welton, E. J., Korkin, S. V., and Lyapustin, A. I.: Advancements in the Aerosol Robotic Network (AERONET) Version 3 database, Atmos. Meas. Tech., 12, 169–209, https://doi.org/10.5194/amt-12-169-2019, 2019.

Huang, J., Minnis, P., Yi, Y., Tang, Q., Wang, X., Hu, Y., Liu, Z., Ayers, K., Trepte, C., and Winker, D.: Summer dust aerosols detected from CALIPSO over the Tibetan Plateau, Geophys. Res. Lett., 34, L18805, https://doi.org/10.1029/2007GL029938, 2007.

Iarlori, M., Madonna, F., Rizi, V., Trickl, T., and Amodeo, A.: Effective resolution concepts for lidar observations, Atmos. Meas. Tech., 8, 5157–5176, https://doi.org/10.5194/amt-8-5157-2015, 2015.

Illingworth, A. J., Barker, H. W., Beljaars, A., Ceccaldi, M., Chepfer, H., Clerbaux, N., Cole, J., Delanoe, J., Domenech, C., Donovan, D. P., Fukuda, S., Hirakata, M., Hogan, R. J., Huenerbein, A., Kollias, P., Kubota, T., Nakajima, T., Nakajima, T. Y., Nishizawa, T., Ohno, Y., Okamoto, H., Oki, R., Sato, K., Satoh, M., Shephard, M. W., Velazquez-Blazquez, A., Wandinger, U., Wehr, T., and van Zadelhoff, G.-J.: The EarthCARE satellite: the next step forward in global measurements of clouds, aerosols, precipitation, and radiation, B. Am. Meteorol. Soc., 96, 1311–1332, https://doi.org/10.1175/BAMS-D-12-00227.1, 2015.

Immerzeel, W. W., van Beek, L. P. H., and Bierkens, M. F. P.: Climate change will affect the Asian water towers, Science, 328, 1382–1385, https://doi.org/10.1126/science.1183188, 2010.

Kim, M.-H., Kim, S.-W., and Omar, A. H.: Quantifying the low bias of CALIPSO's column aerosol optical depth due to undetected aerosol layers, J. Geophys. Res.-Atmos., 122, 1098–1113, https://doi.org/10.1002/2016JD025797, 2017.

Kim, M.-H., Omar, A. H., Tackett, J. L., Vaughan, M. A., Winker, D. M., Trepte, C. R., Hu, Y., Liu, Z., Poole, L. R., Pitts, M. C., Kar, J., and Magill, B. E.: The CALIPSO version 4 automated aerosol classification and lidar ratio selection algorithm, Atmos. Meas. Tech., 11, 6107–6135, https://doi.org/10.5194/amt-11-6107-2018, 2018.

Lau, K. M., Kim, M. K., and Kim, K. M.: Asian summer monsoon anomalies induced by aerosol direct forcing: the role of the Tibetan Plateau, Clim. Dynam., 26, 855–864, https://doi.org/10.1007/s00382-006-0114-z, 2006.

Liu, Z., Kar, J., Zeng, S., Tackett, J., Vaughan, M., Avery, M., Pelon, J., Getzewich, B., Lee, K.-P., Magill, B., Omar, A., Lucker, P., Trepte, C., and Winker, D.: Discriminating between clouds and aerosols in the CALIOP version 4.1 data products, Atmos. Meas. Tech., 12, 703–734, https://doi.org/10.5194/amt-12-703-2019, 2019.

Lu, D., Pan, W., and Wang, Y.: Atmospheric profiling synthetic observation system in Tibet, Adv. Atmos. Sci., 35, 264–267, https://doi.org/10.1007/s00376-017-7251-7, 2018.

Mattis, I., Ansmann, A., Muller, D., Wandinger, U., and Althausen, D.: Multiyear aerosol observations with dual-wavelength Raman lidar in the framework of EARLINET, J. Geophys. Res., 109, D13203, https://doi.org/10.1029/2004JD004600, 2004.

Mattis, I., D'Amico, G., Baars, H., Amodeo, A., Madonna, F., and Iarlori, M.: EARLINET Single Calculus Chain, technical, Part 2: Calculation of optical products, Atmos. Meas. Tech., 9, 3009–3029, https://doi.org/10.5194/amt-9-3009-2016, 2016.

NASA/LARC/SD/ASDC: CALIPSO Lidar Level 2 5 km Aerosol Profile, V4-51 [data set], NASA Langley Atmospheric Science Data Center Distributed Active Archive Center, https://doi.org/10.5067/CALIOP/CALIPSO/CAL_LID_L2_05kmAPro-Standard-V4-51, 2018.

Pappalardo, G., Amodeo, A., Pandolfi, M., Wandinger, U., Ansmann, A., Bosenberg, J., Matthias, V., Amiridis, V., De Tomasi, F., Frioud, M., Iarlori, M., Komguem, L., Papayannis, A., Rocadenbosch, F., and

Wang, X.: Aerosol lidar intercomparison in the framework of the EARLINET project. 3. Raman lidar algorithm for aerosol extinction, backscatter, and lidar ratio, Appl. Optics, 43, 5370–5385, https://doi.org/10.1364/AO.43.005370, 2004.

Pappalardo, G., Amodeo, A., Apituley, A., Comber, A., Freudenthaler, V., Linne, H., Ansmann, A., Bosenberg, J., D'Amico, G., Mattis, I., Mona, L., Wandinger, U., Amiridis, V., Alados-Arboledas, L., Nicolae, D., and Wiegner, M.: EARLINET: towards an advanced sustainable European aerosol lidar network, Atmos. Meas. Tech., 7, 2389–2409, https://doi.org/10.5194/amt-7-2389-2014, 2014.

Pokharel, M., Guang, J., Liu, B., Kang, S., Ma, Y., Holben, B. N., Xia, X., Seemala, G. K., and Peng, G.: Aerosol properties over Tibetan Plateau from a decade of AERONET measurements: baseline, types, and influencing factors, J. Geophys. Res.-Atmos., 124, 13357–13374, https://doi.org/10.1029/2019JD031293, 2019.

Sassen, K. and Cho, B. S.: Subvisual-thin cirrus lidar dataset for satellite verification and climatological research, J. Appl. Meteorol., 31, 1275–1285, https://doi.org/10.1175/1520-0450(1992)031<1275:STCLDF>2.0.CO;2, 1992.

Toth, T. D., Campbell, J. R., Reid, J. S., Tackett, J. L., Vaughan, M. A., Zhang, J., and Marquis, J. W.: Minimum aerosol layer detection sensitivities and their subsequent impacts on aerosol optical thickness retrievals in CALIPSO level 2 data products, Atmos. Meas. Tech., 11, 499–514, https://doi.org/10.5194/amt-11-499-2018, 2018.

Vaughan, M. A., Powell, K. A., Winker, D. M., Hostetler, C. A., Kuehn, R. E., Hunt, W. H., Getzewich, B. J., Young, S. A., Liu, Z., and McGill, M. J.: Fully automated detection of cloud and aerosol layers in the CALIPSO lidar measurements, J. Atmos. Ocean. Tech., 26, 2034–2050, https://doi.org/10.1175/2009JTECHA1228.1, 2009.

Wandinger, U. and Ansmann, A.: Experimental determination of the lidar overlap profile with Raman lidar, Appl. Optics, 41, 511–514, https://doi.org/10.1364/AO.41.000511, 2002.

Wandinger, U., Floutsi, A. A., Baars, H., Haarig, M., Ansmann, A., Hempel, D., Freudenthaler, V., Groiss, S., Mattis, I., Tesche, M., Pappalardo, G., Mona, L., and D'Amico, G.: HETEAC, the Hybrid End-To-End Aerosol Classification model for EarthCARE, Atmos. Meas. Tech., 16, 2485–2510, https://doi.org/10.5194/amt-16-2485-2023, 2023.

Wang, Y., Cui, H., Zhao, W., Bi, Y., Wang, T., and Lu, D.: Multi-wavelength elastic/Raman/depolarisation lidar aerosol dataset from Yangbajing on the interior Tibetan Plateau (2021–2024) [data set], Zenodo, https://doi.org/10.5281/zenodo.21317571, 2026.

Watson-Parris, D., Schutgens, N., Winker, D., Burton, S. P., Ferrare, R. A., and Stier, P.: On the limits of CALIOP for constraining modeled free tropospheric aerosol, Geophys. Res. Lett., 45, 9260–9266, https://doi.org/10.1029/2018GL078195, 2018.

Winker, D. M., Vaughan, M. A., Omar, A., Hu, Y., Powell, K. A., Liu, Z., Hunt, W. H., and Young, S. A.: Overview of the CALIPSO mission and CALIOP data processing algorithms, J. Atmos. Ocean. Tech., 26, 2310–2323, https://doi.org/10.1175/2009JTECHA1281.1, 2009.

https://doi.org/10.5194/essd-2026-552
Preprint. Discussion started: 17 August 2026

Xu, X., Wu, H., Yang, X., and Xie, L.: Distribution and transport characteristics of dust aerosol over the Tibetan Plateau and Taklimakan Desert in China using MERRA-2 and CALIPSO data, Atmos. Environ., 237, 117670, https://doi.org/10.1016/j.atmosenv.2020.117670, 2020.

Yao, T., Thompson, L., Yang, W., Yu, W., Gao, Y., Guo, X., Yang, X., Duan, K., Zhao, H., Xu, B., Pu, J., Lu, A., Xiang, Y., Kattel, D. B., and Joswiak, D.: Different glacier status with atmospheric circulations in Tibetan Plateau and surroundings, Nat. Clim. Change, 2, 663–667, https://doi.org/10.1038/nclimate1580, 2012.

Zhang, M., Yan, H., Miao, Y., Wang, Y., Chen, S., Zhao, T., and Du, P.: Evaluation of reanalysis 3-D aerosol products against CALIPSO measurements over the Tibetan Plateau, Atmos. Res., 322, 108126, https://doi.org/10.1016/j.atmosres.2025.108126, 2025.

Zhao, W., Wang, Y., Bi, Y., Wu, X., Tian, Y., Qiu, Y., and Pan, Y.: Unveiling cloud vertical structures over the interior Tibetan Plateau through anomaly detection in synergetic lidar and radar observations, Adv. Atmos. Sci., 41, 2381–2398, https://doi.org/10.1007/s00376-024-3221-z, 2024.